

1 **Rheologic constraints on the upper mantle from five years of**
2 **postseismic deformation following the El Mayor-Cucapah**
3 **earthquake**

4 **T. T. Hines¹, E. A. Hetland¹**

5 ¹Department of Earth and Environmental Sciences, University of Michigan, Ann Arbor, Michigan, USA.

6 **Key Points:**

- 7 • Transient postseismic deformation can be observed following the El Mayor-Cucapah
8 earthquake at epicentral distances of up to 400 km
9 • Near-field postseismic deformation exhibits early transience that decays to a sustained
10 rate which is elevated above the preseismic trend
11 • Far-field postseismic deformation can be explained with a Zener or Burgers rheology
12 upper mantle

13 **Abstract**

14 We analyze five years of Southern California GPS data following the Mw=7.2 El Mayor-Cucapah
 15 earthquake. We observed transient postseismic deformation which persists for three years at
 16 epicentral distances greater than ~ 200 km. In the near-field, rapid postseismic transience de-
 17 cays to a sustained rate which exceeds its preseismic trend. We attempt to determine the mech-
 18 anisms driving this deformation, where we consider afterslip at seismogenic depths and vis-
 19 coelastic relaxation in the lower crust and upper mantle as candidate mechanisms. We find that
 20 early, rapid, near-field deformation can be explained with afterslip on the fault that ruptured
 21 coseismically. The later, sustained, near-field deformation can be explained with viscoelastic
 22 relaxation in the lower crust with a steady-state viscosity of $\sim 10^{19}$ Pa s and possibly contin-
 23 ued afterslip. The later postseismic deformation in the far-field is best explained with a tran-
 24 sient viscosity of $\sim 10^{18}$ Pa s in the upper mantle. We argue that a transient rheology in the
 25 mantle is preferable over a Maxwell rheology because it better predicts the decay in postseis-
 26 mic deformation, and also because it does not conflict with the generally higher, steady-state
 27 viscosities inferred from studies of geophysical processes occurring over longer time scales.

28 **1 Introduction**

29 Ground deformation in the years following a large ($Mw \gtrsim 7$) earthquake can be used to
 30 gain insight into the mechanical behavior of the crust and upper mantle. The interpretations
 31 of postseismic deformation are not always conclusive because multiple postseismic deforma-
 32 tion mechanisms, such as afterslip or viscoelastic relaxation in the lower crust and upper man-
 33 tle, can have qualitatively similar surface expressions [e.g. Savage, 1990]. This non-uniqueness
 34 complication can potentially be remedied if the postseismic deformation occurs in an area that
 35 is sufficiently well instrumented with GPS stations [Hearn, 2003]. Owing to the dense geode-
 36 tic network deployed throughout the 2000s as part of the Plate Boundary Observatory, the post-
 37 seismic deformation following the April 4, 2010, Mw=7.2 El Mayor-Cucapah earthquake in
 38 Baja California was observed at more GPS stations than any other earthquake in California
 39 to date (see Hauksson *et al.* [2011] and Fletcher *et al.* [2014] for a detailed description of this
 40 earthquake and its seismotectonic context). With such a large collection of data, we attempt
 41 to discern the mechanisms driving the postseismic deformation.

42 Previous studies which have modeled postseismic deformation following the El Mayor-
 43 Cucapah earthquake include Pollitz *et al.* [2012], Gonzalez-Ortega *et al.* [2014], Spinler *et al.*
 44 [2015], and Rollins *et al.* [2015]. Of these studies, Gonzalez-Ortega *et al.* [2014] and Rollins
 45 *et al.* [2015] have attempted to describe the postseismic deformation with afterslip in an elas-
 46 tic half-space. Gonzalez-Ortega *et al.* [2014] described five months of postseismic deforma-
 47 tion, observed by InSAR and GPS stations within ~ 50 km of the rupture, with afterslip and
 48 contraction on the coseismically ruptured fault. Gonzalez-Ortega *et al.* [2014] noted that their
 49 preferred model underestimated the GPS displacements for stations $\gtrsim 25$ km from the rup-
 50 ture and suggested that it could be the result of unmodeled viscoelastic relaxation. Using only
 51 continuous GPS stations, which are mostly north of the rupture zone, Rollins *et al.* [2015] found
 52 that three years of postseismic deformation can be adequately explained by afterslip, albeit with
 53 an implausibly large amount of slip inferred on the least constrained, southern-most fault seg-
 54 ment. Here, we suggest the afterslip inferred by Rollins *et al.* [2015] may have been acting as
 55 a proxy for distributed relaxation in the upper mantle.

56 Pollitz *et al.* [2012], Rollins *et al.* [2015] and Spinler *et al.* [2015] explored viscoelastic
 57 relaxation in the lower crust and upper mantle as a potential postseismic deformation mech-
 58 anism. The rheology of the crust and mantle is largely unknown and so modeling postseis-
 59 mic deformation with viscoelastic relaxation requires one to assume a rheologic model and
 60 then find the best fitting rheologic parameters. The inference of these rheologic parameters is
 61 a computationally expensive non-linear inverse problem which is typically approached with
 62 a forward modeling grid search method. Consequently, a simplified structure for the Earth must
 63 be assumed in order to minimize the number of rheologic parameters that need to be estimated.

For example, it is commonly assumed that the lower crust and upper mantle are homogeneous, Maxwell viscoelastic layers, which may be too simplistic for postseismic studies [Riva and Govers, 2009; Hines and Hetland, 2013]. To further reduce the dimensions of the model space, it is also necessary to make simplifying assumptions about the behavior of afterslip. For example, one can assume a frictional model for afterslip and parametrize afterslip in terms of the unknown rheologic properties of the fault [e.g. Johnson *et al.*, 2009; Johnson and Segall, 2004]. One can also assume that afterslip does not persist for more than a few months and then model the later postseismic deformation assuming it to be the result of only viscoelastic relaxation [e.g. Pollitz *et al.*, 2012; Spiner *et al.*, 2015]. However, afterslip in similar tectonic settings has been observed to persist for decades following earthquakes [Çakir *et al.*, 2012; Cetin *et al.*, 2014]. Indeed, the preferred viscoelastic model from Pollitz *et al.* [2012] significantly underestimates deformation in the Imperial Valley, which could be indicative of unmodeled continued afterslip. Neglecting to allow for sustained afterslip as a postseismic mechanism could then lead to biased inferences of viscosities.

In this study, we perform a kinematic inversion for fault slip, allowing it to persist throughout the postseismic period, while simultaneously estimating the viscosity of the lower crust and upper mantle. We create an initial model of the fault slip and effective viscosity necessary to describe early postseismic deformation using the method described in Hines and Hetland [2016]. This method uses a first-order approximation of surface deformation resulting from viscoelastic relaxation which is only applicable to the early postseismic period. In this case, our initial model describes the first 0.8 years of postseismic deformation following the El Mayor-Cucapah earthquake. We then use the inferred effective viscosity structure from the initial model to create a suite of postseismic models which we test against the five years of postseismic data available to date. Of the suite of models tested, we find that postseismic deformation following the El Mayor-Cucapah earthquake can be explained with a combination of afterslip on a fault segment running through the Sierra Cucapah and viscoelastic relaxation in a Zener rheology upper mantle with a transient viscosity on the order of 10^{18} Pa s.

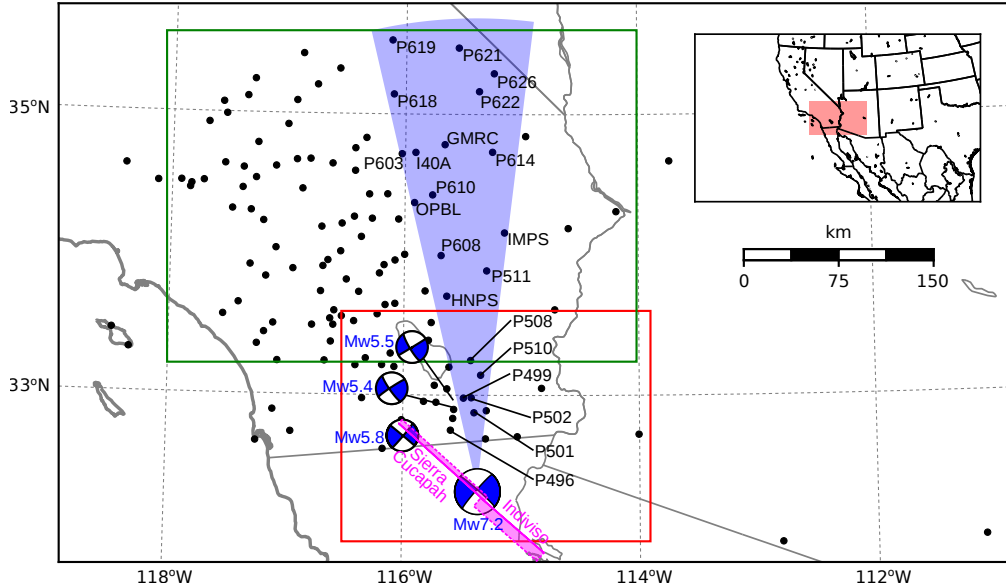
2 Data Processing

We use continuous GPS position time series provided by University Navstar Consortium (UNAVCO) for stations within a 400 km radius about the El Mayor-Cucapah epicenter. We collectively describe the coseismic and postseismic displacements resulting from the El Mayor-Cucapah earthquake as $u_{\text{post}}(t)$. We consider the GPS position time series, $u_{\text{obs}}(t)$, to be the combination of $u_{\text{post}}(t)$, secular tectonic deformation, annual and semi-annual oscillations, and coseismic offsets from significant earthquakes over the time span of this study. The June 14, 2010, Mw=5.8 Ocotillo earthquake and the Brawley swarm, which included an Mw=5.5 and an Mw=5.4 event on August 26, 2012 (Figure 1), are the only earthquakes that produced noticeable displacements in any of the time series. We treat the displacements resulting from the Brawley swarm as a single event because the daily solutions provided by UNAVCO cannot resolve the separate events. Although the Ocotillo earthquake had its own series of aftershocks [Hauksson *et al.*, 2011], neither the Ocotillo earthquake nor the Brawley swarm produced detectable postseismic deformation. We model displacements resulting from these events with only a Heaviside function, $H(t)$, describing the coseismic offsets. We then model $u_{\text{obs}}(t)$ as

$$u_{\text{obs}}(t) = u_{\text{pred}}(t) + \epsilon, \quad (1)$$

where

$$\begin{aligned} u_{\text{pred}}(t) = & u_{\text{post}}(t)H(t - t_{\text{emc}}) + c_0 + c_1 t + \\ & c_2 \sin(2\pi t) + c_3 \cos(2\pi t) + c_4 \sin(4\pi t) + c_5 \cos(4\pi t) + \\ & c_6 H(t - t_{\text{oc}}) + c_7 H(t - t_{\text{bs}}). \end{aligned} \quad (2)$$



91 **Figure 1.** Map of the region considered in this study. The large focal mechanism is the GCMT solution
 92 for the El Mayor-Cucapah earthquake, and the three small focal mechanisms are for the Ocotillo earthquake
 93 and the two main shocks during the Brawley swarm. The black dots indicate the locations of GPS stations
 94 used in this study. The fault geometry used in this study is shown in magenta where dashed lines indicate
 95 buried edges of the fault segments. The green and red boxes demarcate the extent of the near-field and far-
 96 field maps (Figures 4 and 5). Stations inside the blue sector, which highlights the area within 10° of the El
 97 Mayor-Cucapah P-axis, are used in Figures 7 and 10.

114 In the above equations, t_{emc} , t_{oc} and t_{bs} are the times of the El Mayor-Cucapah earthquake,
 115 Ocotillo earthquake, and the Brawley swarm, respectively, c_0 through c_7 are unknown coef-
 116 ficients, and ϵ is the observation noise. We are using years as our unit of time which makes
 117 c_2 through c_5 the coefficients for annual and semi-annual oscillations. We only estimate jumps
 118 associated with the Ocotillo earthquake and Brawley swarm for stations within 40 km of their
 119 epicenters.

120 Stations which recorded displacements that clearly cannot be described by the aforemen-
 121 tioned processes are not included in our analysis. This includes stations in the Los Angeles
 122 basin, where anthropogenic deformation can be larger than the postseismic signal that we are
 123 trying to estimate [Bawden *et al.*, 2001; Argus *et al.*, 2005]. In order to ensure an accurate es-
 124 timation of the secular deformation, we only use stations that were installed at least six months
 125 prior to El Mayor-Cucapah earthquake even though several GPS stations were installed after
 126 the earthquake to get better coverage of the postseismic deformation field [Spiner *et al.*, 2015].
 127 It would be possible to subtract secular velocities derived from elastic block models [e.g. Meade
 128 and Hager, 2005] from velocities recorded at the newly installed stations to get an estimate
 129 of postseismic velocities at those stations. However, estimating velocities from an already noisy
 130 displacement time series can introduce significant uncertainties depending on exactly how the
 131 estimation is done. We therefore use coseismic and postseismic displacements, rather than ve-
 132 locities, in our inverse method described in Section 3. This choice prevents us from using the
 133 newly installed stations for our analysis.

134 The October 16, 1999, Mw=7.1 Hector Mine earthquake, which occurred \sim 270 km north
 135 of the El Mayor-Cucapah epicenter, produced transient postseismic deformation which we do
 136 not wish to model, either mechanically or through empirical line fitting. We thus restrict our
 137 analysis to deformation observed six years after the Hector Mine earthquake, which is when

138 postseismic velocities at sites near the Hector Mine epicenter are approximately constant [Savage
 139 and Svare, 2009]. When appraising our model fit in Section 3, we see some systematic
 140 residuals in the vicinity of the Hector Mine epicenter, which may be the result of errors in the
 141 assumption that the trend in Hector Mine postseismic deformation is linear after six years.

142 Studies of postseismic deformation typically assume a parametric form for $u_{\text{post}}(t)$, such
 143 as one with a logarithmic or exponential time dependence [e.g. Savage *et al.*, 2005]. However,
 144 by assuming a logarithmic or exponential form of $u_{\text{post}}(t)$ we run the risk of over fitting the
 145 GPS time series and inferring a non-existent postseismic signal. We therefore do not assume
 146 any parametric form for $u_{\text{post}}(t)$ and rather treat it as integrated Brownian motion, so that

$$\dot{u}_{\text{post}}(t) = \sigma^2 \int_0^t w(s) ds, \quad (3)$$

147 where $w(t)$ is white noise and the variance of $\dot{u}_{\text{post}}(t)$ increases linearly with time by a factor
 148 of σ^2 . We use a Kalman filtering approach to estimate $u_{\text{post}}(t)$ and the unknown parameters in eq. (2). In the context of Kalman filtering, our time varying state vector is
 149

$$\mathbf{X}(t) = [u_{\text{post}}(t), \dot{u}_{\text{post}}(t), c_0, \dots, c_7] \quad (4)$$

150 and eq. (2) is the observation function which maps the state vector to the GPS observations.
 151 We initiate the Kalman filter by assuming a prior estimate of $\mathbf{X}(t)$ at the first time epoch, denoted
 152 $\mathbf{X}_{1|0}$, which has a sufficiently large covariance, denoted $\Sigma_{1|0}$, to effectively make our
 153 prior uninformed. For each time epoch, t_i , Bayesian linear regression is used to incorporate
 154 GPS derived estimates of displacement with our prior estimate of the state, $\mathbf{X}_{i|i-1}$, to form
 155 a posterior estimate of the state, $\mathbf{X}_{i|i}$, which has covariance $\Sigma_{i|i}$. We then use the posterior
 156 estimate of the state at time t_i to form a prior estimate of the state at time t_{i+1} through the
 157 transition function

$$\mathbf{X}_{i+1|i} = \mathbf{F}_{i+1} \mathbf{X}_{i|i} + \delta_{i+1}, \quad (5)$$

158 where

$$\mathbf{F}_{i+1} = \begin{bmatrix} 1 & (t_{i+1} - t_i) & \mathbf{0} \\ 0 & 1 & \mathbf{0} \\ \mathbf{0} & \mathbf{0} & \mathbf{I} \end{bmatrix} \quad (6)$$

159 and δ_{i+1} is the process noise, which has zero mean and covariance described by

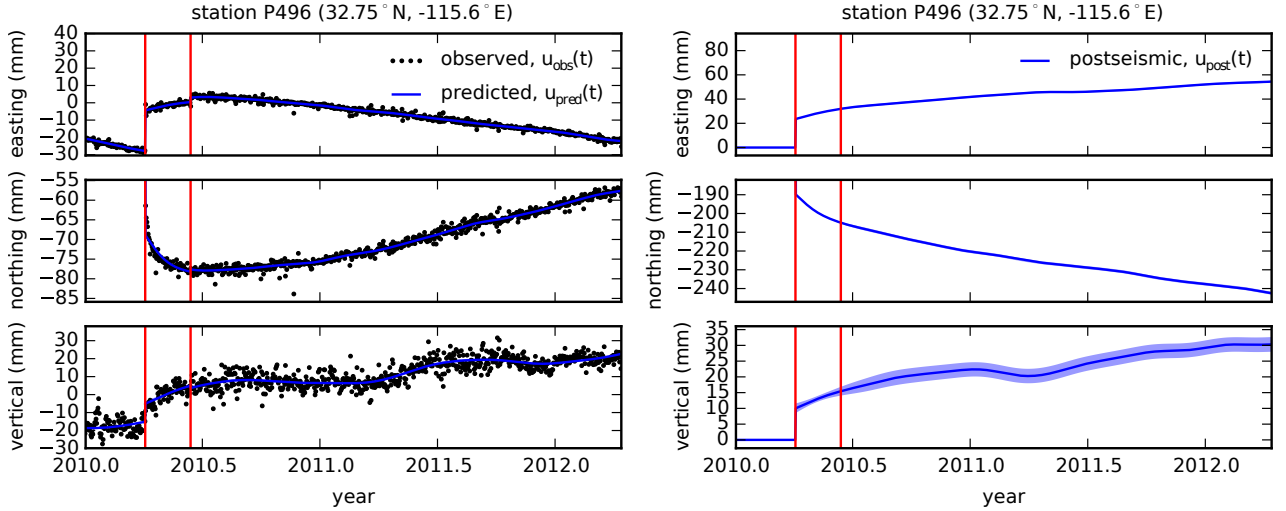
$$\mathbf{Q}_{i+1} = \sigma^2 \begin{bmatrix} \frac{(t_{i+1} - t_i)^3}{3} & \frac{(t_{i+1} - t_i)^2}{2} & \mathbf{0} \\ \frac{(t_{i+1} - t_i)^2}{2} & (t_{i+1} - t_i) & \mathbf{0} \\ \mathbf{0} & \mathbf{0} & \mathbf{0} \end{bmatrix}. \quad (7)$$

160 The covariance of the new prior state, $\mathbf{X}_{i+1|i}$, is then described by

$$\Sigma_{i+1|i} = \mathbf{F}_{i+1} \Sigma_{i|i} \mathbf{F}_{i+1}^T + \mathbf{Q}_{i+1}. \quad (8)$$

161 This process is repeated for each of the N time epochs. We then use Rauch-Tung-Striebel smoothing
 162 [Rauch *et al.*, 1965] to find $\mathbf{X}_{i|N}$, which is an estimate of the state at time t_i that incor-
 163 porates GPS observation for all N time epochs. Our final estimates of $u_{\text{post}}(t)$ are used in sub-
 164 sequent analysis, while the remaining components of the state vector are considered nuisance
 165 parameters. In the interests of computational tractability, we down sample our smoothed time
 166 series from daily solutions down to weekly solutions.

167 The smoothness of $u_{\text{post}}(t)$ is controlled by the chosen value of σ^2 , which describes how
 168 rapidly we expect postseismic displacements to vary over time. Setting σ^2 equal to zero will



185 **Figure 2.** Left panels show GPS time series from UNAVCO (black) and the predicted displacement (blue)
 186 from eq. (2) for a near-field station. Red lines indicate the times of the El Mayor-Cucapah and Ocotillo earth-
 187 quake. The right panels show estimated coseismic and postseismic displacements, u_{post} , which are extracted
 188 from the predicted displacements. The 68% confidence interval is shown in light blue.

169 effectively result in modeling $u_{\text{post}}(t)$ as a straight line which is insufficient to describe the
 170 expected transient behavior in postseismic deformation. The other end member, where σ^2 is
 171 infinitely large, will result in $u_{\text{pred}}(t)$ overfitting the data. While one can use a maximum like-
 172 lihood based approach for picking σ^2 [e.g. Segall and Mathews, 1997], we instead take a sub-
 173 jective approach and choose a value for σ^2 that is just large enough to faithfully describe the
 174 observed deformation at the most near-field station in our study, P496, which exhibits the most
 175 rapid changes in velocity. This ensures that σ^2 will be sufficiently large so that our estimate
 176 of $u_{\text{post}}(t)$ does not smooth out potentially valuable postseismic signal at the remaining sta-
 177 tions. We find that using $\sigma^2 = 0.05 \text{ m}^2/\text{yr}^3$ adequately describes all but the first week of post-
 178 seismic deformation at station P496, which slightly increases our estimate of coseismic dis-
 179 placements (Figure 2). We include an example of estimating $u_{\text{post}}(t)$ for a far-field station,
 180 P619, which is about 359 km north of the El Mayor-Cucapah epicenter (Figure 3). At station
 181 P619, along with all the other stations in the Mojave region, there is a south-trending post-
 182 seismic transience that persists for the first three years after the El Mayor-Cucapah earthquake.
 183 Postseismic deformation that extends to these epicentral distances has also been observed af-
 184 ter the Hector Mine earthquake [Freed et al., 2007].

190 It is important to note that the shown uncertainties in $u_{\text{post}}(t)$ do not account for the non-
 191 negligible epistemic uncertainty in eq. (2). For example, we assume a constant rate of secu-
 192 lar deformation, which appears to be an appropriate approximation for all but perhaps the sta-
 193 tions closest to the Hector Mine epicenter, as noted above. Also, our model for seasonal de-
 194 formation in eq. (2) assumes a constant amplitude over time, which means that any yearly vari-
 195 ability in the climatic conditions could introduce systematic residuals [Davis et al., 2012]. In-
 196 deed, it would be more appropriate to consider the seasonal amplitudes $c_2 - c_5$ in eq. (2) as
 197 stochastic variables [Murray and Segall, 2005]. By using constant seasonal amplitudes, our es-
 198 timate of $u_{\text{post}}(t)$ seems to describe some of the unmodeled annual and semi-annual oscilla-
 199 tions (e.g. Figure 3).

200 We show in Figures 4 and 5 the near and far-field coseismic displacements and the post-
 201 seismic displacements accumulated over the time intervals 0–1 years, 1–3 years, and 3–5 years.
 202 Stations at epicentral distances beyond ~ 200 km have an elevated rate of deformation for the
 203 first three years following the earthquake. This far-field deformation is trending southward at

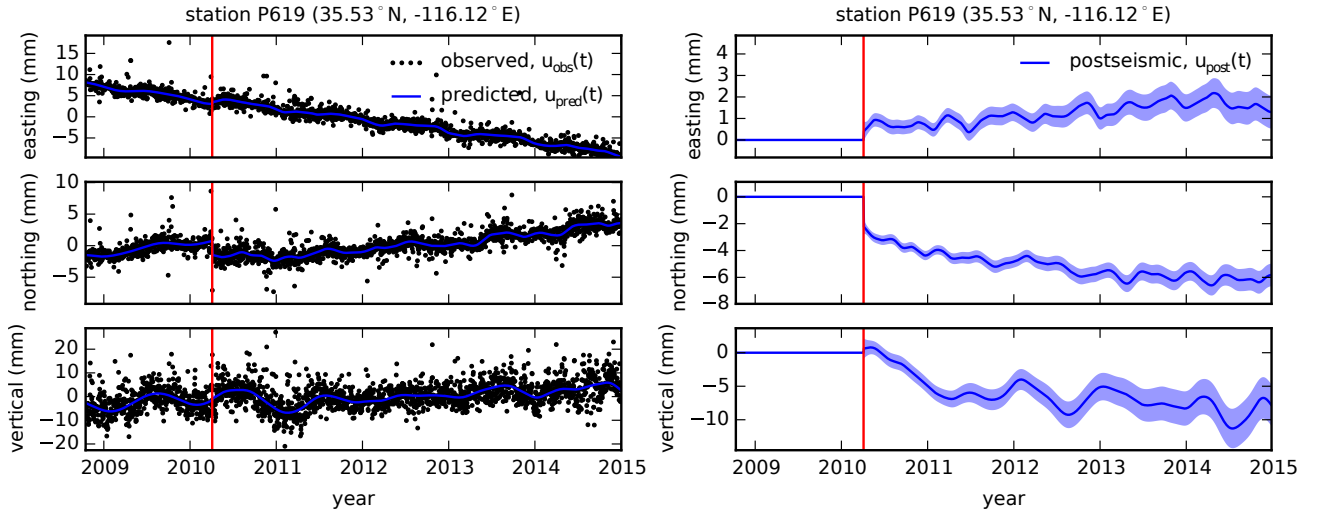


Figure 3. same as Figure 2 but for a far-field station.

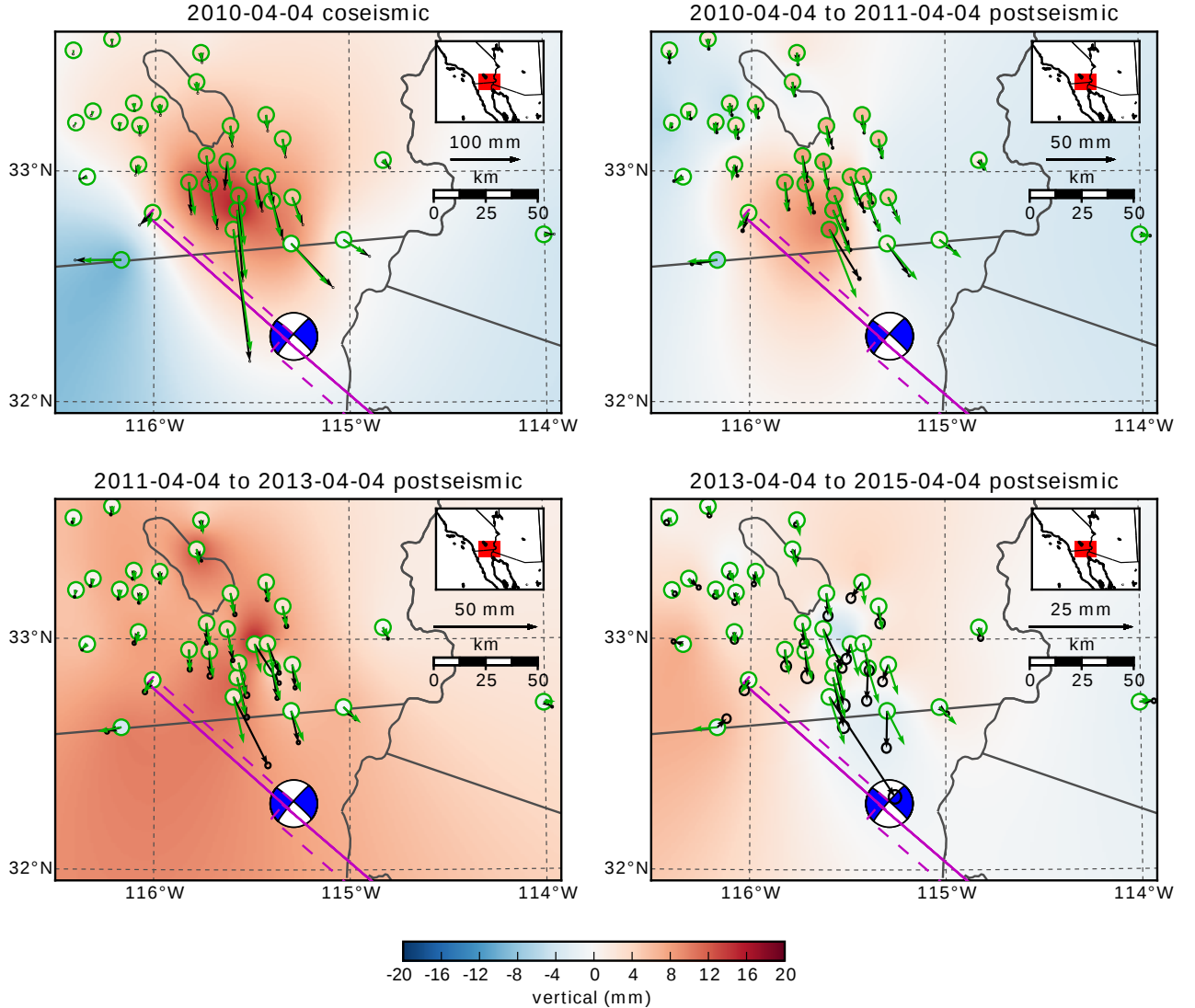
a rate of a few millimeters per year along the direction of the El Mayor-Cucapah P-axis. A similar eastward trend can be seen in the few far-field stations in Arizona, located along the T-axis. After three years, the trend in far-field postseismic deformation is barely perceptible. Most far-field stations display an initial subsidence for the first year after the El Mayor-Cucapah earthquake followed by continued uplift. This trend in vertical deformation can be observed in all three of the quadrants where postseismic data is available, which means that the vertical deformation does not exhibit an anti-symmetric quadrant pattern, as would be expected for postseismic processes. Although we use vertical deformation in our analysis in Section 3, we do not put an emphasis on trying to describe the vertical deformation because it likely does not have postseismic origins.

The near-field postseismic deformation is notably sustained when compared to the far-field deformation. Namely, the station in this study which is closest to the El Mayor-Cucapah epicenter, P496, has a steady postseismic trend of ~ 1.5 cm/yr to the south after about one year. Vertical postseismic deformation in the near-field does display a quadrant pattern which is consistent with the coseismic vertical deformation, suggesting that it is resulting from postseismic processes. However, the vertical postseismic signal is only apparent for the first year after the earthquake (Figure 4). As with the far-field deformation, there is a general trend of uplift in the near-field after about one year.

3 Postseismic Modeling

We seek to find the mechanisms driving five years of postseismic deformation following the El Mayor-Cucapah earthquake and we consider afterslip and viscoelastic relaxation as candidate mechanisms. Poroelastic rebound has also been used to model postseismic deformation [e.g. Jónsson *et al.*, 2003]; however, Gonzalez-Ortega *et al.* [2014] found that poroelastic rebound is unlikely to be a significant contributor to postseismic deformation following the El Mayor-Cucapah earthquake. Furthermore, we consider stations which are sufficiently far away from the rupture that poroelastic rebound should be insignificant.

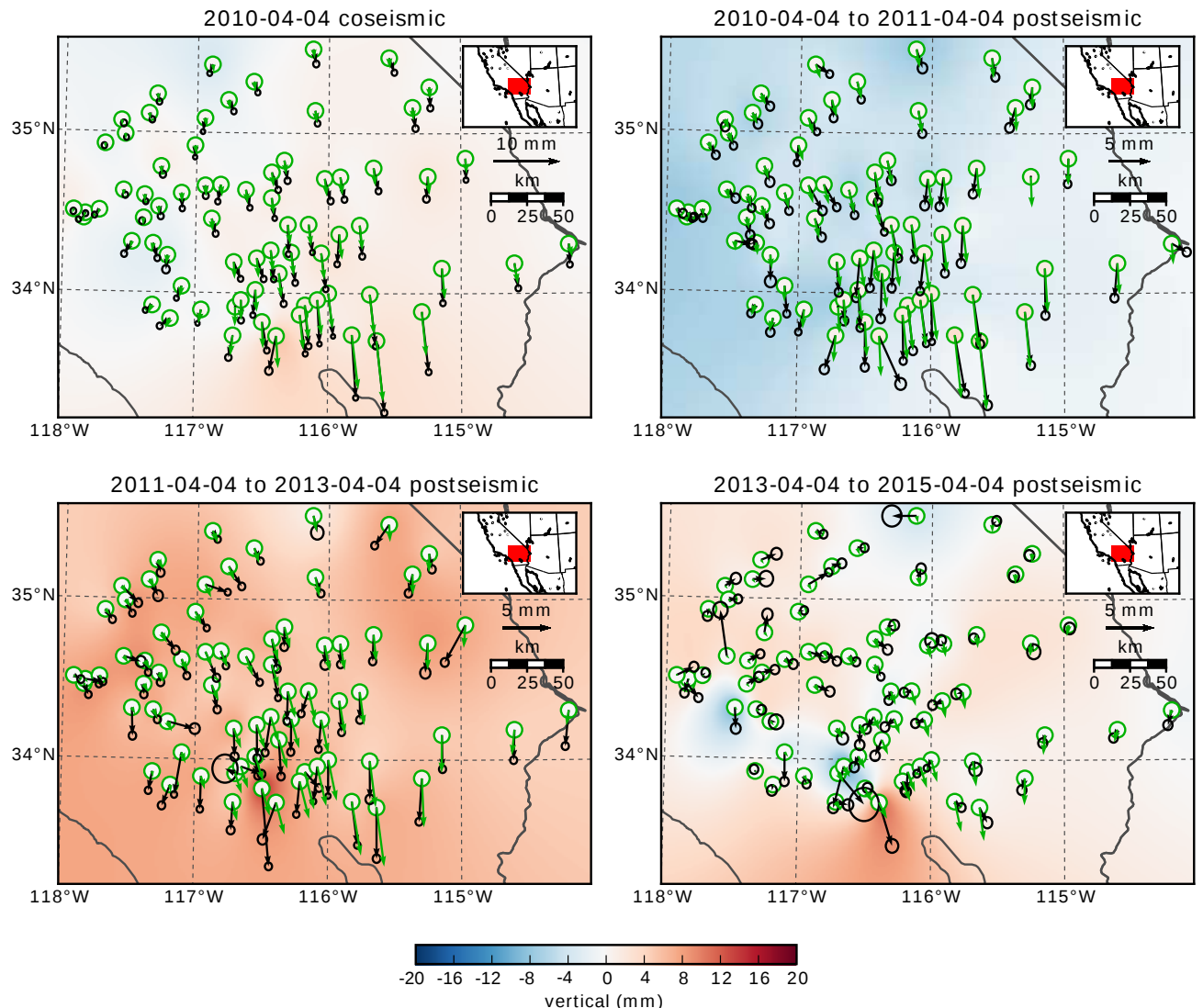
We estimate coseismic and time-dependent postseismic fault slip, both of which are assumed to occur on a fault geometry modified from Wei *et al.* [2011b]. Field studies [Fletcher *et al.*, 2014] and LIDAR observations [Oskin *et al.*, 2012] have revealed a significantly more complicated fault geometry than what was inferred by Wei *et al.* [2011b], especially within the Sierra Cucapah. However, we find that a relatively simple coseismic fault geometry based on



214 **Figure 4.** Near-field coseismic and cumulative postseismic displacements over the indicated time periods
 215 (black) and predicted displacements for our preferred model from Section 3.3 (green). The black error ellipses
 216 show the 68% confidence interval for the observed horizontal displacements. Observed vertical displacements
 217 are shown as an interpolated field and predicted vertical displacements are shown within the green circles.
 218 Note that the interpolant is not well constrained in Mexico where there is no data available.

depth (km)	λ (GPa)	μ (GPa)	η_{eff} (10^{18} Pa s)	μ_k/μ
0-5	24.0	24.0	-	-
5-15	35.0	35.0	-	-
15-30	42.0	42.0	44.3	0.0
30-60	61.0	61.0	5.91	0.375
60-90	61.0	61.0	1.99	0.375
90-120	61.0	61.0	1.31	0.375
120-150	61.0	61.0	1.10	0.375
150-∞	61.0	61.0	1.07	0.375

229 **Table 1.** Assumed and estimated material properties. λ and μ are assumed known *a priori* and are based
 230 on the values used for the coseismic model by Wei *et al.* [2011b]. The values for η_{eff} are estimated in Section
 231 3.2, and μ_k/μ are the optimal shear moduli ratios found in Section 3.3 for a Zener rheology upper mantle.

**Figure 5.** Same as Figure 4 but for far-field stations.

219

[Wei *et al.*, 2011b] is adequate because most of the stations used in this study are sufficiently far from the El Mayor-Cucapah rupture that they are insensitive to the details in the fault geometry found by Fletcher *et al.* [2014] and Osokin *et al.* [2012]. The fault geometry used in this study (Figure 1) consists of the two main fault segments inferred by Wei *et al.* [2011b], where the northern segment runs through the Sierra Cucapah up to the US-Mexico border and the southern segment is the Indiviso fault which extends down to the Gulf of California. Both segments extend from the surface to 15 km depth. We extend the northern segment by 40 km to the northwest, which is motivated by the clustering of aftershocks on the northern tip of the coseismic rupture zone [Hauksson *et al.*, 2011; Kroll *et al.*, 2013]. This extended fault segment was also found to be necessary by Rollins *et al.* [2015] and Pollitz *et al.* [2012] in order to describe the postseismic deformation.

255 3.1 Elastic Postseismic Inversion

We consider a variety of rheologic models for the lower crust and upper mantle. The simplest rheologic model is to consider them to be effectively elastic and isotropic. In such case, the rheologic parameters consist of the reasonably well known Lamé parameters, λ and μ , and we use the same values used by Wei *et al.* [2011b] throughout this paper (Table 1). The only unknown is the distribution of fault slip, which can be estimated from postseismic deformation through linear least squares. Rollins *et al.* [2015] used a subset of the GPS stations considered in this study and found that three years of postseismic deformation following the El Mayor-Cucapah earthquake can be explained with afterslip on the coseismic fault plane without requiring any viscoelastic relaxation. We also perform an elastic slip inversion, but we use GPS stations within a larger radius about the El Mayor-Cucapah epicenter (400 km instead of \sim 200 km). Our forward problem describing predicted postseismic deformation, u_{pred} , in terms of time dependent fault slip, s , is

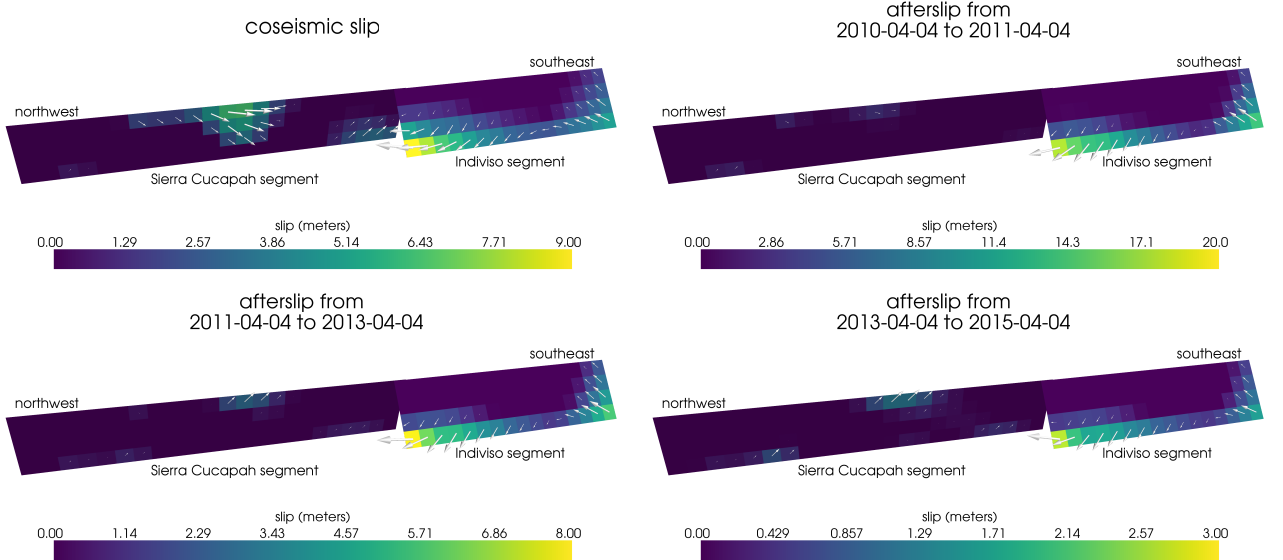
$$267 u_{\text{pred}}(x, t) = \int_F s(\xi, t) g(x, \xi) d\xi, \quad (9)$$

where F denotes the fault and $g(x, \xi)$ is the elastic Green's function describing displacement at surface position x resulting from slip at ξ on the fault. We estimate coseismic slip and the rate of afterslip over the postseismic time intervals 0.0-0.125, 0.125-0.25, 0.25-0.5, 0.5-1.0, 1.0-2.0, 2.0-3.0, 3.0-4.0, and 4.0-5.0 years. Each fault segment is discretized into roughly 4 km by 4 km patches and we impose that the direction of slip and slip rate are within 45° of right-lateral. We also add zeroth-order Tikhonov regularization so that our solution for s satisfies

$$274 \min_s \left(\left\| \frac{u_{\text{pred}}(s) - u_{\text{post}}}{\sigma_{\text{post}}} \right\|_2^2 + \lambda_s \|s\|_2^2 \right), \quad (10)$$

where σ_{post} is the uncertainty on postseismic displacements and λ_s is a penalty parameter which is chosen with a trade-off curve. We use Pylith [Aagaard *et al.*, 2013] to compute the Green's functions for this inversion as well as for the remaining inversions in this paper.

Our coseismic slip and afterslip solutions are shown in Figure 6. Similar to Rollins *et al.* [2015], we find that a large amount of afterslip on the Indiviso fault segment is required to explain the observations. The potency of our inferred coseismic slip is $3.2 \times 10^9 \text{ m}^3$, equivalent to a Mw=7.28 earthquake when assuming a shear modulus of 32 GPa. The potency of our inferred cumulative five years of afterslip is $6.1 \times 10^9 \text{ m}^3$, equivalent to a Mw=7.46 earthquake, which is unrealistically large if we consider afterslip to be driven by coseismically induced stresses. Figure 7 shows the time series for the observed and predicted postseismic displacements at stations along the El Mayor-Cucapah P-axis. We show the radial component of displacements with respect to the El Mayor-Cucapah epicenter and we also rescale the displacements so that the difference between the minimum and maximum observed displacements are the same for each station. Our elastic slip model accurately describes near-field postseis-



294 **Figure 6.** Coseismic slip and cumulative afterslip over the indicated time intervals when assuming the crust
295 and mantle are elastic. Color indicates the magnitude of slip and arrows indicate the motion of the hanging
296 wall.

297 mic deformation and systematically underestimates postseismic deformation at epicentral dis-
298 tances $\gtrsim 150$ km. When the fault segments used in the inversion are extended down to 30 km
299 depth, rather than 15 km, the systematic far-field residuals are smaller but remain apparent.
300 Because an elastic model requires an unrealistic amount of afterslip and is unable to predict
301 far-field deformation, we move on to consider viscoelastic models in the next section.

306 3.2 Early Postseismic Inversion

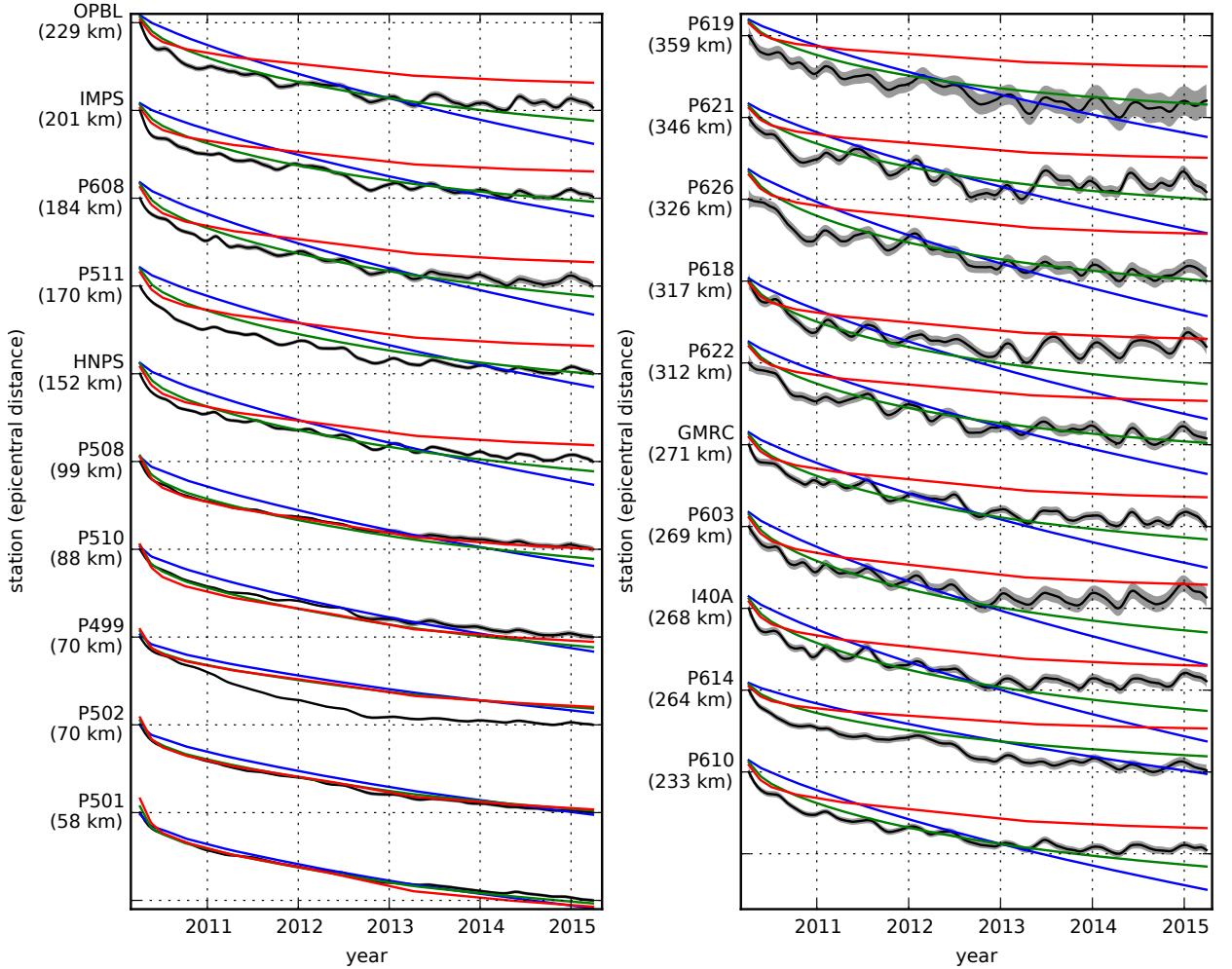
307 For any linear viscoelastic rheology of the crust and mantle, postseismic displacements
308 resulting from time dependent fault slip can be described as

$$u_{\text{pred}}(x, t) = \int_F s(\xi, t) g(x, \xi) d\xi + \int_0^t \int_F s(\xi, \tau) f(t - \tau, x, \xi) d\xi d\tau, \quad (11)$$

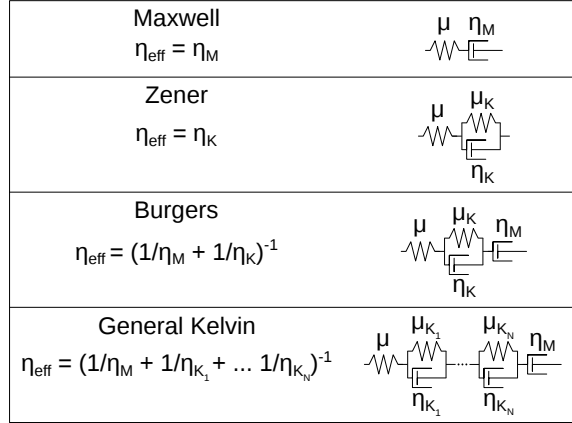
309 where $f(t, x, \xi)$ describes the time-dependent velocity at x resulting from viscoelastic relax-
310 ation of stresses induced by slip at ξ . f is a function of λ , μ , and any additional rheologic pa-
311 rameters controlling the viscoelastic response, which are generally not well known. Schematic
312 representations of the viscoelastic rheologic models considered in this study are shown in Fig-
313 ure 8. We discuss these rheologic models and their use in geophysical studies in Section 4.

314 In order to greatly simplify the inverse problem, we use the method described in *Hines*
315 and *Hetland* [2016] to constrain an initial effective viscosity structure from the early postseis-
316 mic deformation. Our method uses the fact that coseismic stresses throughout the crust and
317 upper mantle depend on the instantaneous elastic parameters and are independent of the vis-
318 coelastic parameters which we wish to estimate. Immediately following an earthquake, each
319 parcel will have a strain rate that is proportional to the coseismic stress and inversely propor-
320 tional to the parcel's effective viscosity, η_{eff} . Using one-dimensional rheologic models, we de-
321 fine the effective viscosity as
322

$$\eta_{\text{eff}} = \left. \frac{\sigma}{\dot{\varepsilon}} \right|_{t=0}, \quad (12)$$



297 **Figure 7.** Scaled radial component of postseismic displacements. Downward motion indicates that the
 298 station is moving toward the El Mayor-Cucapah epicenter. Displacement time series are scaled so that the
 299 minimum and maximum observed values lie on the grid lines. The observed postseismic displacements, u_{post}
 300 are shown in black with gray indicating the 68% confidence interval. The displacements predicted by the best
 301 fitting elastic model are shown in red. The blue and green lines are the predicted postseismic displacements
 302 for the models discussed in Section 3.3. The blue lines show the predicted displacements for the model with
 303 a Maxwell viscoelastic lower crust and upper mantle. The green line shows the predicted displacements for
 304 our preferred model, which has a Maxwell viscoelastic lower crust and a Zener viscoelastic upper mantle. The
 305 effective viscosities are the same for both models and are shown in Figure 12.



314 **Figure 8.** Schematic illustration of the rheologic models considered in this paper as well as their effective
 315 viscosities.

324 where σ is an applied stress at $t = 0$ and $\dot{\varepsilon}$ is the resulting strain rate. Figure 8 shows how
 325 η_{eff} relates to the parameters for various linear viscoelastic rheologies. We can deduce that the
 326 initial rate of surface deformation resulting from viscoelastic relaxation is a summation of the
 327 surface deformation resulting from relaxation in each parcel, scaled by the reciprocal of the
 328 parcel's effective viscosity. That is to say

$$f(0, x, \xi) = \int_L \frac{h(x, \xi, \zeta)}{\eta_{\text{eff}}(\zeta)} d\zeta, \quad (13)$$

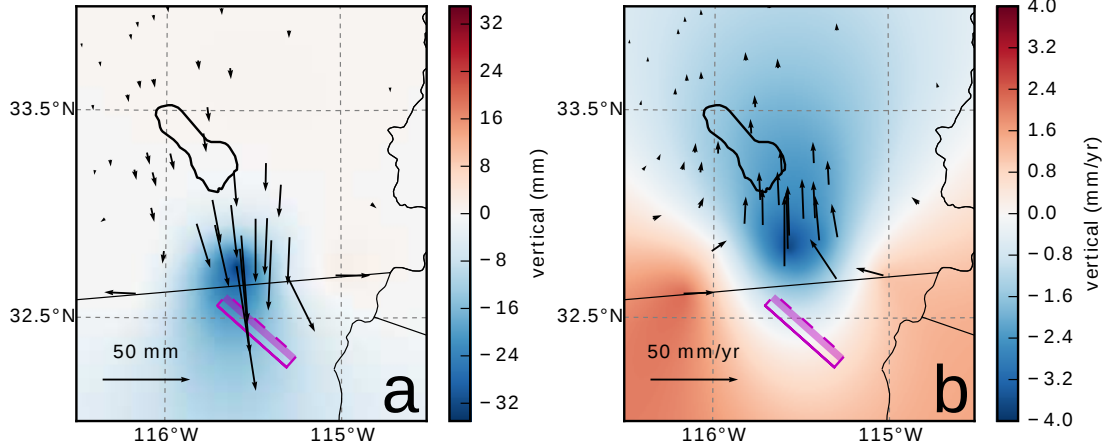
329 where L denotes the crust and mantle and $h(x, \xi, \zeta)$ describes the initial rate of deformation
 330 resulting from viscoelastic relaxation at ζ induced by slip at ξ . We can combine eq. (13) with
 331 eq. (11) to get a first-order approximation for early postseismic deformation,

$$u_{\text{pred}}(x, t) \approx \int_F s(\xi, t) g(x, \xi) d\xi + \int_0^t \int_F \int_L \frac{s(\tau, \xi)}{\eta_{\text{eff}}(\zeta)} h(x, \xi, \zeta) d\zeta d\xi d\tau, \quad (14)$$

332 which is valid for as long as the rate of deformation resulting from viscoelastic relaxation is
 333 approximately constant. Although eq. (14) may only be valid for a short portion of the post-
 334 seismic period, its utility becomes apparent when noting that g and h are only functions of
 335 the fault geometry and instantaneous elastic properties, λ and μ , and thus g and h can be com-
 336 puted numerically as a preprocessing step. The forward problem in eq. (14) can then be rapidly
 337 evaluated for any realization of s and η_{eff} . This is in contrast to evaluating the full forward
 338 problem, eq. (11), numerically for each realization of s and the unknown rheologic proper-
 339 ties.

340 Details on how eq. (14) is used to estimate s and η_{eff} from postseismic deformation can
 341 be found in *Hines and Hetland* [2016]. A non-linear Kalman filter based inverse method can
 342 also be used to estimate s and η_{eff} in a manner similar to *Segall and Mathews* [1997] or *McGuire*
 343 and *Segall* [2003], in which we would not have to explicitly impose a time dependent parametriza-
 344 tion of s . We have thoroughly explored Kalman filter based approaches, but we ultimately pre-
 345 fer the method described in *Hines and Hetland* [2016] because of its relative simplicity. More-
 346 over, we believe the piecewise continuous representation of slip with respect to time is suf-
 347 ficiently general for the resolving power of these GPS data.

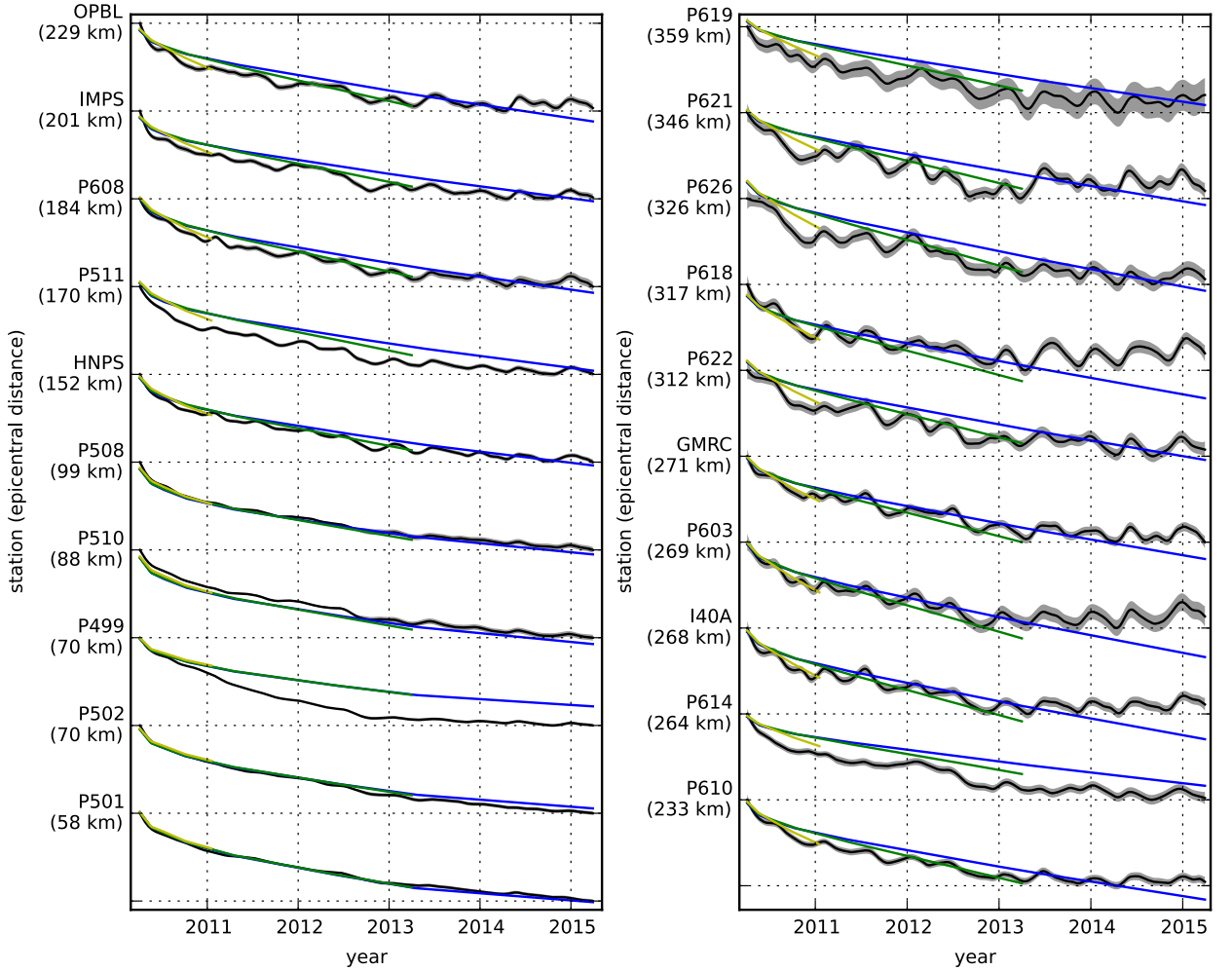
348 We estimate coseismic slip and afterslip with the same spatial and temporal discretiza-
 349 tion as in Section 3.1. Simultaneously, we estimate η_{eff} within six vertically stratified layers
 350 which have depths ranging from 15–30 km, 30–60 km, 60–90 km, 90–120 km, 120–150 km,



370 **Figure 9.** Displacements resulting from fault slip at lower crustal depths (a), and initial velocities resulting
 371 from subsequent relaxation of a viscoelastic lower crust (b). The fault segment dips 75° to the north-east and
 372 its surface projection is outlined in magenta. The highlighted area on the fault extends from 15 to 30 km depth
 373 and indicates where 1 meter of right-lateral slip was imposed. The elastic properties of the crust and mantle
 374 are the same as in Table 1, and η_{eff} is 10^{18} Pa s in the lower crust. Vertical displacements are interpolated
 375 between station locations.

351 and from 150 km to the bottom of our numerical model domain at 800 km. We again restrict
 352 fault slip to occur between 0 and 15 km depth, which is done in order to help eliminate in-
 353 evitable non-uniqueness in the inversion. It is well understood that fault slip at sufficiently great
 354 depths can produce surface deformation that is indistinguishable from viscoelastic relaxation,
 355 at least in two-dimensional earthquake models [Savage, 1990]. Additionally, we note that when
 356 simultaneously estimating both afterslip and viscosity in the lower crust, the inverse problem
 357 becomes particularly ill-posed. This ill-posedness is illustrated in Figure 9, which shows the
 358 displacements resulting from a meter of slip on a fault extending from 15 to 30 km depth and
 359 the initial velocity resulting from subsequent viscoelastic relaxation in the lower crust, which
 360 is given a viscosity of 10^{18} Pa s. In this demonstration, the viscoelastic relaxation is entirely
 361 driven by the fault slip in the lower crust. The horizontal displacements from fault slip are in
 362 the opposite direction as the displacements resulting from viscoelastic relaxation. This means
 363 that surface displacements resulting from afterslip at lower crustal depths can be cancelled out,
 364 at least partially, by a low viscosity lower crust. We eliminate this null space by allowing only
 365 one mechanism in the lower crust, which we choose to be viscoelastic relaxation. This is not
 366 to say that we do not believe deep afterslip is a possibility; rather, we restrict slip to seismo-
 367 genic depths as a modeling necessity. Although, it has been noted that the pattern of vertical
 368 postseismic deformation following the El Mayor-Cucapah earthquake indicates that a signif-
 369 icant amount of afterslip must be shallow [Rollins *et al.*, 2015].

376 We must determine at which point the early postseismic approximation breaks down, which
 377 we will denote as t_{bd} . As noted, eq. (14) is valid for as long as the rate of deformation re-
 378 sulting from viscoelastic relaxation is approximately constant. We can almost certainly assume
 379 that deformation at the most far-field stations, which are ~ 400 km away from the El Mayor-
 380 Cucapah epicenter, is the result of viscoelastic relaxation. The approximation should then be
 381 valid for as long as a linear trend adequately approximates the far-field deformation. Using
 382 this logic, it would appear that t_{bd} is about one year after the El Mayor-Cucapah earthquake.
 383 Another way to determine t_{bd} is to find the best fitting prediction of eq. (14) to observed de-
 384 formation using increasing durations of the postseismic time series. t_{bd} should be the point
 385 when eq. (14) is no longer capable of describing the observed deformation without incurring
 386 systematic misfits. When using eq. (14) to fit the entire five years of postseismic displacements,



398 **Figure 10.** Observed postseismic displacements (black) and best fitting predictions of eq. (14) to 5.0 (blue),
 399 3.0 (green), and 0.8 (yellow) years of the postseismic data.

387 we see that the near-field displacements (e.g., station P501) are accurately predicted. When
 388 looking at displacements in the far-field (e.g., station P621), we see that eq. (14) overestimates
 389 the rate of deformation in the later postseismic period and underestimates the rate of defor-
 390 mation in the early period (Figure 10). Due to the low signal-to-noise ratios for far-field sta-
 391 tions, it is difficult to determine at what point eq. (14) is no longer able to predict the observed
 392 displacements; however, we settle on $t_{bd} = 0.8$ years after the earthquake, while acknowl-
 393 edging that the choice is subjective. As noted in *Hines and Hetland* [2016], overestimating t_{bd}
 394 will result in a bias towards overestimating η_{eff} , while picking a t_{bd} which is too low will not
 395 necessarily result in a biased estimate of η_{eff} , although the uncertainties would be larger. We
 396 can then consider inferences of η_{eff} to be an upper bound on the viscosity needed to describe
 397 the far-field rate of deformation during the first 0.8 years of postseismic deformation.

400 We estimate coseismic slip, afterslip, and effective viscosities by solving

$$\min_{s, \eta_{eff}} \left(\left\| \frac{u_{pred}(s, \eta_{eff}) - u_{post}}{\sigma_{post}} \right\|_2^2 + \lambda_s \|s\|_2^2 + \lambda_\eta \|\nabla \eta_{eff}^{-1}\|_2^2 \right), \quad (15)$$

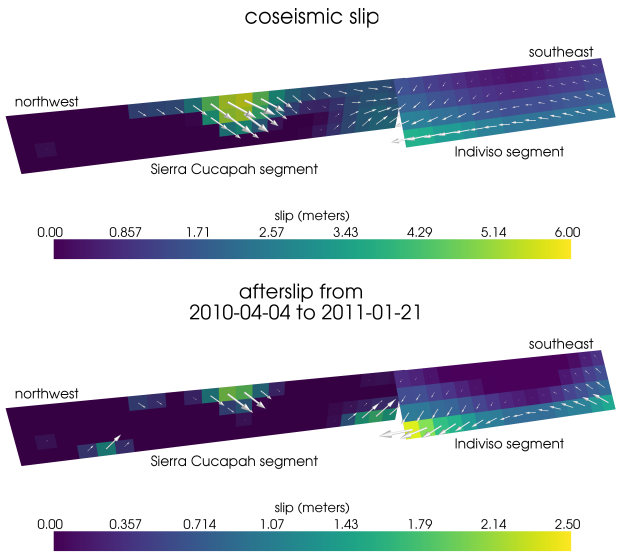
401 where u_{post} consists of the first 0.8 years of postseismic deformation and u_{pred} are the pre-
 402 dicted displacements from eq. (14). Due to inherent non-uniqueness, we have added zeroth-
 403 order Tikhonov regularization to estimates of s and second-order Tikhonov regularization to
 404 estimates of effective fluidity η_{eff}^{-1} . The degree to which we impose the regularization on slip
 405 and fluidity is controlled by the penalty parameters λ_s and λ_η , which are chosen with trade-
 406 off curves (Figure S1). Our goal is to get a prior constraint on η_{eff} to minimize the amount
 407 of searching we have to do when describing the postseismic deformation over the full five years,
 408 which we do in Section 3.3. Estimates of s made here will not be used in Section 3.3, and
 409 so the motivation behind adding regularization to s is to ensure that the slip driving viscoelas-
 410 tic relaxation in eq. (14) is sensible.

411 Our initial estimate for coseismic slip and cumulative afterslip over the first 0.8 years
 412 after the El Mayor-Cucapah earthquake are shown in Figure 11. Similar to our elastic slip model
 413 from Section 3.1, a significant amount of right-lateral and normal coseismic slip is inferred
 414 to be on the Sierra Cucapah segment. Our coseismic slip solution on the Sierra Cucapah seg-
 415 ment is consistent with field studies [Fletcher *et al.*, 2014] and the model from Wei *et al.* [2011b].
 416 Our inferred slip on the Indiviso fault segment differs from Wei *et al.* [2011b] because the GPS
 417 data used in this study is not capable of resolving the spatial distribution of fault slip on that
 418 segment (Figure S2). The potency of inferred coseismic slip is $3.3 \times 10^9 \text{ m}^3$, which is also
 419 about the same as that inferred from Section 3.1. The present inference of afterslip on the In-
 420 diviso fault is significantly less than what was found in the Section 3.1 where we did not ac-
 421 count for viscoelasticity. When fault slip is simultaneously estimated with viscosity, the po-
 422 tency of inferred afterslip over the first 0.8 years after the earthquake is $0.85 \times 10^9 \text{ m}^3$, com-
 423 pared to $3.5 \times 10^9 \text{ m}^3$ when we assume the crust and upper mantle are elastic. The signifi-
 424 cant amount of afterslip inferred on the Indiviso fault in Section 3.1 seems to be compensat-
 425 ing for unmodeled viscoelastic relaxation. The fact that there is still an appreciable amount
 426 of afterslip inferred on the Indiviso fault raises the question of whether it is compensating for
 427 viscoelastic relaxation that is more localized than what we allow for since we only estimate
 428 depth dependent variations in viscosity.

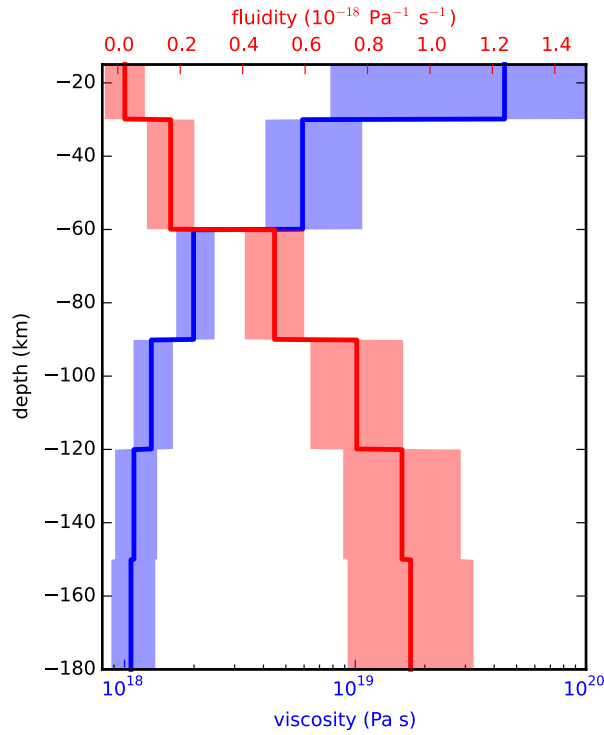
429 Our estimated effective viscosities, and corresponding fluidities, are shown in Figure 12.
 430 Although fluidity is rarely used in geophysical literature, eq. (13) is linear with respect to flu-
 431 idity and so the fluidity indicates the amplitude of the viscoelastic signal coming from each
 432 layer. We use bootstrapping to find the 95% confidence intervals for our estimated effective
 433 viscosities which are shown as shaded regions in Figure 12. It is important to remember that
 434 the presented effective viscosities were estimated with a smoothing regularization constraint
 435 and so the uncertainties are almost certainly underestimated [Aster *et al.*, 2011]. Indeed, many
 436 viscosity profiles which are outside of the shown confidence intervals can just as adequately
 437 described the first 0.8 years of postseismic deformation. Our solution in Figure 12 should be
 438 interpreted as the smoothest effective viscosity profile which is capable of describing the data.
 439 This means that any sharp viscosity transitions will be tapered out in the inversion, which we
 440 demonstrate with a synthetic test in Figure S2. Nonetheless, a robust feature that we see with
 441 a variety of choices for λ_s , λ_η , and t_{bd} is that the largest jump in fluidity is at 60 km depth,
 442 which is consistent with the range of lithosphere-asthenosphere boundary depths inferred by
 443 Lekic *et al.* [2011]. This transitional depth is also consistent with the the viscosity structure
 444 required to explain far-field postseismic deformation following the Hector Mine earthquake
 445 [Freed *et al.*, 2007]. We find that the viscosity below 60 km depth needs to be $\sim 1 \times 10^{18} \text{ Pa}$
 446 s to describe the early rate of postseismic deformation at far-field stations while the lower crust
 447 and uppermost mantle need to be relatively stronger. The viscosity of the lower crust has the
 448 largest uncertainties because there is no evidence of relaxation in that layer, meaning that it
 449 is effectively elastic over the first 0.8 years after the earthquake.

455 3.3 Full Postseismic Inversion

456 In the previous section, we used the inverse method from Hines and Hetland [2016] to
 457 constrain the effective viscosity structure required to explain the first 0.8 years of postseismic



450 **Figure 11.** Coseismic slip and afterslip inferred by fitting eq. (14) to the first 0.8 years of postseismic
451 displacements.



452 **Figure 12.** Effective viscosities and associated fluidities inferred by fitting eq. (14) to the first 0.8 years of
453 postseismic displacements. 95% confidence intervals, estimated from bootstrapping, are indicated by shaded
454 regions.

458 deformation. In this section, we use these effective viscosities as a prior constraint when searching
 459 for models which are capable of describing the available five years of postseismic data,
 460 where our forward problem is now eq. (11) rather than the approximation given by eq. (14).
 461 We perform a series of fault slip inversions assuming a variety of rheologies for the lower crust
 462 and upper mantle which are consistent with our findings from Section 3.2. We appraise each
 463 model using the mean chi-squared value,

$$\bar{\chi}^2 = \frac{1}{N} \left\| \frac{u_{\text{pred}} - u_{\text{post}}}{\sigma_{\text{post}}} \right\|_2^2, \quad (16)$$

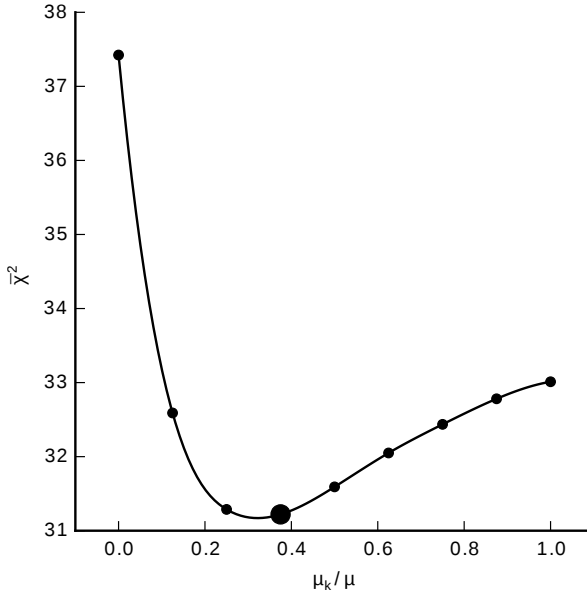
464 where N is the number of observations.

465 We first assume that the crust and mantle can be described with a Maxwell rheology,
 466 and we set the steady-state viscosity, η_M , equal to our inference of η_{eff} . We compute f and
 467 g from eq. (11) using Pylith, and we use the same spatial and temporal discretization of s as
 468 in Sections 3.1 and 3.2. We estimate s using linear least squares and find a misfit of $\bar{\chi}^2 =$
 469 37.4. For comparison, $\bar{\chi}^2 = 35.3$ for the elastic model from Section 3.1. The Maxwell vis-
 470 coelastic model has a larger misfit because it tends to overestimate the rate of deformation af-
 471 ter about three years (Figure 7). Since our initial estimates of η_{eff} may be biased towards over-
 472 estimating viscosities, we have also performed the slip inversion where we use uniformly lower
 473 viscosities in the crust and mantle; however, decreasing the viscosity only increases the mis-
 474 fit. Although, the viscosities used here are consistent with the successful Maxwell viscoelas-
 475 tic models found by *Rollins et al.* [2015] and *Spinler et al.* [2015], which had mantle viscosi-
 476 ties on the order of 10^{18} Pa s and relatively higher lower crustal viscosities, we find that such
 477 a model is incapable of describing the entire postseismic time series. *Pollitz et al.* [2001] sim-
 478 ilarly recognized this deficiency in a Maxwell rheology, which then motivated their exploration
 479 of a Burgers rheology upper mantle [*Pollitz*, 2003].

480 Instead of exploring a Burgers rheology mantle, which introduces two new parameters
 481 that need to be estimated, the transient viscosity, η_K , and transient shear modulus, μ_K , we first
 482 consider a Zener rheology for the mantle, which only introduces one unknown model param-
 483 eter, μ_K . We assume that the lower crust still has a Maxwell rheology. The steady-state vis-
 484 cosity in the crust and the transient viscosity in the mantle are set equal to the inferred effec-
 485 tive viscosities. We then estimate the ratio of shear moduli, $\frac{\mu_K}{\mu}$. We compute nine different
 486 sets of Green's functions, f and g , where we assume values of $\frac{\mu_K}{\mu}$ ranging from 0 to 1. The
 487 former being a degenerate case where the Zener model reduces to the above Maxwell model.
 488 We estimate coseismic slip and afterslip for each realization of $\frac{\mu_K}{\mu}$. We find that a shear mod-
 489 uli ratio of 0.375 yields the best prediction to the observed postseismic displacements with a
 490 misfit of $\bar{\chi}^2 = 31.2$ (Figure 13). The improvement in the Zener model over the Maxwell model
 491 can be seen in the fit to the far-field data (Figure 7) where the Zener model does a significantly
 492 better job at explaining the transient rate of deformation throughout the five years considered
 493 in this study. The rheologic parameters for our preferred Zener model are summarized in Ta-
 494 ble 1.

497 Because we are able to adequately describe the available five years of postseismic de-
 498 formation with a Zener model, we do not find it necessary to explore the parameter space for
 499 a more complicated Burgers rheology. However, since the Zener model is a Burgers model with
 500 an infinite steady-state viscosity, we can conclude that any Burgers rheology that has a tran-
 501 sient viscosity consistent with that found in Section 3.2 and a steady-state viscosity $\gtrsim 10^{20}$
 502 Pa s, which is effectively infinite on the time scale of five years, would also be able to sat-
 503 isfactorily describe the observable postseismic deformation.

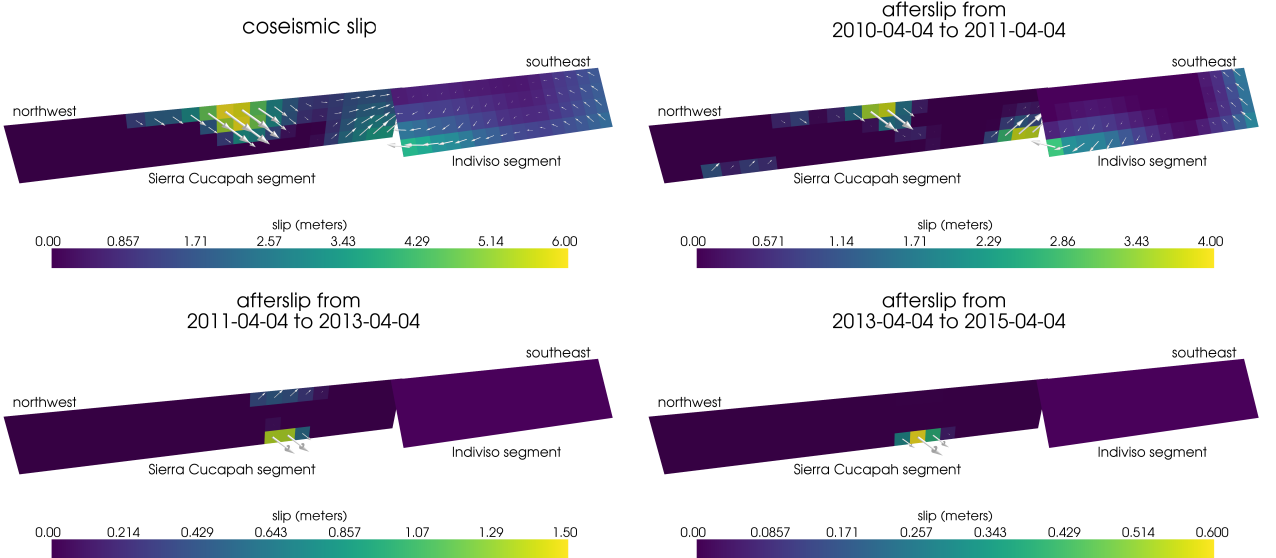
504 The regularized inference of coseismic slip and afterslip for our preferred Zener model
 505 is shown in Figure 14. The inferred coseismic potency is 3.0×10^9 m³, equivalent to a Mw=7.26
 506 earthquake, where most of the slip is shallow and on the Sierra Cucapah fault segment. The
 507 potency of five years of afterslip is 1.1×10^9 m³. Most of the afterslip in our preferred model
 508 occurs within the first year after the earthquake and coincides with the location of our inferred



495 **Figure 13.** Mean chi-squared value as a function of the transient shear modulus relative to the elastic shear
 496 modulus in a Zener rheology upper mantle. Large dot indicates our preferred ratio.

509 coseismic slip. Inferred afterslip within the first year is accounting for the most rapid near-
 510 field transient deformation (Figure S3). After one year, afterslip is inferred to be deeper down
 511 on the Sierra Cucapah segment. The sustained near-field postseismic deformation is being ex-
 512 plained by this continued afterslip as well as viscoelastic relaxation in the lower crust. We em-
 513 phasize, that the GPS station closest to where we infer afterslip, P496, is still about 30 km away,
 514 which is too far for us to conclusively discern deep afterslip from viscoelastic relaxation in
 515 the lower crust. The deep afterslip inferred after one year could potentially be compensating
 516 for an overestimated lower crustal viscosity. To test this, we have modified our preferred model
 517 by decreasing the lower crustal viscosity from 5.91×10^{19} Pa s to 1×10^{19} Pa s, which is
 518 still consistent with our viscosity inference from Section 3.2, and we inverted for fault slip.
 519 We find that a model with a weaker lower crust adequately describes the postseismic displace-
 520 ments without any afterslip after one year, while still requiring about the same amount of af-
 521 terslip over the first year. We do believe that the early afterslip on the Sierra Cucapah segment
 522 is a robust feature in our preferred model, while we are not confident in our inference of later
 523 deep afterslip.

524 The postseismic displacements predicted by our preferred Zener model are shown in Fig-
 525 ures 4, 5 and 7. The largest misfit occur within the Imperial Valley where there does not ap-
 526 pear to be any systematic trend in the residuals. This suggests that the large errors are due to
 527 localized processes such as fault slip in the Imperial Valley triggered by the El Mayor-Cucapah
 528 earthquake [Wei *et al.*, 2011a, 2015]. We do not see any pattern in the residuals that would sug-
 529 gest a laterally heterogeneous viscosity structure, which has been explored by Pollitz *et al.* [2012]
 530 and Rollins *et al.* [2015]. We do notice regional scale seasonal oscillations in the lateral and
 531 vertical components of the residuals with an amplitude of 1-2 millimeters. This is the result
 532 of our method for data processing which is not able to completely remove the seasonal sig-
 533 nal in the GPS data, which was discussed in Section 2. Additionally, we see systematic mis-
 534 fit in the later postseismic period west of the Landers and Hector Mine earthquakes, which may
 535 be the result of unmodeled postseismic deformation following those earthquakes. Lastly, there
 536 are clear discrepancies between the observed and predicted vertical displacements following
 537 the first year after the El Mayor-Cucapah earthquake. We observe a broad uplift throughout
 538 Southern California which is inconsistent with any postseismic model.



539 **Figure 14.** Inferred coseismic slip and afterslip for our preferred model, which has a Maxwell rheology
 540 in the lower crust and a Zener rheology in the upper mantle. The transient viscosity, η_K , in the mantle
 541 and steady-state viscosity, η_M , in the crust are set equal to the effective viscosities from Figure 12. We use
 542 $\frac{\mu_K}{\mu} = 0.375$ in the upper mantle.

543 4 Discussion

544 It has long been recognized that deep afterslip and viscoelastic relaxation following an
 545 upper crustal earthquake can result in similar horizontal ground deformation at the surface [e.g.
 546 *Savage*, 1990; *Pollitz et al.*, 2001; *Hearn*, 2003; *Feigl and Thatcher*, 2006]. The similarity of
 547 the horizontal postseismic deformation results in a non-uniqueness in inferences of afterslip
 548 or viscoelastic relaxation. The spatial pattern of vertical postseismic deformation has been pro-
 549 posed to be a discriminant between deep afterslip and viscoelastic relaxation [e.g. *Pollitz et al.*,
 550 2001; *Hearn*, 2003]. It is, however, important to note that patterns of vertical deformation are
 551 very sensitive to the depth-dependence of viscosity below the upper crust [*Yang and Toksöz*,
 552 1981; *Hetland and Zhang*, 2014]. The similarity between deformation resulting from deep af-
 553 terslip and viscoelastic relaxation of coseismic stresses is different from the ill-posedness de-
 554 scribed in Section 3.2. In our method, any inferred afterslip will also mechanically drive ad-
 555 dditional viscoelastic relaxation. The horizontal deformation resulting from deep afterslip will
 556 generally be in the opposite direction as horizontal deformation resulting from viscoelastic re-
 557 laxation of subsequent stresses in the lower crust (Figure 9). As a result, there is a trade-off
 558 between inferences of deep afterslip and lower crustal viscosity. In our synthetic tests in *Hines*
 559 and *Hetland* [2016], we have found that inverting surface deformation for afterslip and vis-
 560 cosity within the same depth interval tends to result in overestimated afterslip and an under-
 561 estimated viscosity.

562 Most postseismic studies assume Maxwell viscoelasticity in the lower crust and upper
 563 mantle [e.g. *Nur and Mavko*, 1974; *Pollitz et al.*, 2000; *Hetland*, 2003; *Freed et al.*, 2006; *John-*
 564 *son et al.*, 2009; *Hearn et al.*, 2009], which is the simplest viscoelastic rheologic model. In South-
 565 ern California, postseismic studies following the Landers [*Pollitz et al.*, 2000], Hector Mine
 566 [*Pollitz et al.*, 2001], and El Mayor-Cucapah earthquake [*Spinler et al.*, 2015; *Rollins et al.*, 2015],
 567 have assumed Maxwell viscoelasticity in the lower crust and upper mantle and have inferred
 568 upper mantle viscosities on the order of 10^{17} to 10^{18} Pa s and lower crust viscosities $\gtrsim 10^{19}$
 569 Pa s. These postseismic studies are consistent with *Kaufmann and Amelung* [2000] and *Cav-*

570 alié *et al.* [2007], who found that an upper mantle viscosity of 10^{18} Pa s and a crustal viscosity
 571 $\gtrsim 10^{20}$ Pa s are necessary to describe subsidence resulting from changes in loading from
 572 Lake Mead. This isostatic adjustment is a process with similar spatial and temporal scales as
 573 postseismic deformation, and thus the inferred viscosities of these two types of studies would
 574 likely agree. While these studies found viscosities that are consistent with our effective vis-
 575 cosities from Section 3.2, they are inconsistent with viscosity estimates made from geophys-
 576 ical processes that occur over longer time scales. For example, Lundgren *et al.* [2009] found
 577 that lower crust and upper mantle viscosities on the order of 10^{21} and 10^{19} Pa s, respectively,
 578 are needed to describe interseismic deformation along the Southern San Andreas fault zone
 579 in the Salton Sea region. An even higher mantle viscosity, on the order of 10^{20} Pa s, is re-
 580 quired to describe isostatic adjustment resulting from the draining of Lake Bonneville, which
 581 occurs on the time scales of 10^4 years [Crittenden, 1967; Bills and May, 1987].

582 An additional deficiency with the Maxwell rheology is that it predicts a steady decay
 583 in the rate of postseismic deformation over time, which fails to describe the commonly ob-
 584 served rapid, early transience followed by a relatively steady rate of postseismic deformation.
 585 One could explain the early transient postseismic deformation with fault creep and the later
 586 phase with relaxation in a Maxwell viscoelastic lower crust and upper mantle [e.g Hearn *et al.*,
 587 2009; Johnson *et al.*, 2009]. However, postseismic deformation at distances greater than ~ 200
 588 km from the El Mayor-Cucapah epicenter can only be attributed to viscoelastic relaxation [e.g.
 589 Freed *et al.*, 2007] and we have demonstrated that the far-field deformation cannot be explained
 590 with a Maxwell rheology (Figure 7).

591 We found that a Zener rheology in the upper mantle with a transient viscosity of $\sim 10^{18}$
 592 Pa s does a noticeably better job at predicting far-field postseismic deformation. A general-
 593 ization of the Zener viscoelastic model, schematically represented as several Kelvin elements
 594 connected in series, is commonly used to describe seismic attenuation [Liu *et al.*, 1976]. The
 595 highest viscosity needed to describe seismic attenuation is on the order of 10^{16} Pa s [Yuen and
 596 Peltier, 1982] which has a characteristic relaxation time on the order of days. Even though
 597 our inferred transient viscosity is orders of magnitude larger than that required for seismic at-
 598 tenuation models, the two models are not incompatible. Rather, the delayed elasticity in seis-
 599 mic attenuation models occurs on such short time scales that it can be considered part of the
 600 instantaneous elastic phase of deformation associated with the preferred Zener model in this
 601 study.

602 Of course, a Zener rheology provides an incomplete description of the asthenosphere be-
 603 cause it does not have the fluid-like behavior required to explain isostatic rebound or convec-
 604 tion in the mantle [O'Connell, 1971]. Yuen and Peltier [1982] proposed a Burgers rheology
 605 with a low transient viscosity ($\eta_K \approx 10^{16}$ Pa s) and high steady-state viscosity ($\eta_M \approx 10^{21}$
 606 Pa s) to describe both seismic attenuation and long term geologic processes. The justification
 607 of a Burger's rheology mantle is further supported by laboratory experiments on olivine [Chopra,
 608 1997]. Pollitz [2003] sought to describe postseismic deformation following Hector Mine with
 609 a Burgers rheology mantle and they found a best fitting transient viscosity of 1.6×10^{17} Pa
 610 s and steady-state viscosity of 4.6×10^{18} Pa s. While the Burgers rheology was introduced
 611 as a means of bridging the gap between relaxation observed in long and short term geophys-
 612 ical processes, the inferred steady state viscosity from Pollitz [2003] is still inconsistent with
 613 the Maxwell viscosities inferred from studies on the earthquake cycle and Lake Bonneville.
 614 The transient viscosity inferred by Pollitz [2003] is constrained by the earliest phase of post-
 615 seismic deformation following the Hector Mine earthquake. While Pollitz [2003] ruled out deep
 616 afterslip as an alternative mechanism based on inconsistent vertical deformation, it is still pos-
 617 sible to successfully describe all components of early postseismic deformation following the
 618 Hector Mine earthquake with afterslip at seismogenic depths [Jacobs *et al.*, 2002]. It is then
 619 possible that the preferred rheologic model from Pollitz [2003] was biased towards inferring
 620 a particularly low transient viscosity by neglecting to account for afterslip. This is in contrast
 621 to the present study, where we have inferred a viscosity structure simultaneously with after-
 622 slip. We also argue that a transient rheology is necessary to explain postseismic deformation;

however, our preferred transient viscosity of $\sim 10^{18}$ Pa s in the upper mantle is an order of magnitude larger than the transient viscosity found by Pollitz [2003]. The transient viscosity inferred here is consistent with the results of Pollitz [2015], who reanalyzed postseismic data following the Landers and Hector Mine earthquake allowing the first few months of transient deformation to be described by afterslip. Since a Zener model is able to describe the available postseismic deformation following the El Mayor-Cucapah earthquake, any Burgers rheology with a steady-state viscosity that is $\gtrsim 10^{20}$ Pa s, effectively infinite over five years, would also be able to describe the postseismic deformation. Such a Burgers model might then be consistent with the steady-state viscosities necessary for lake loading, interseismic deformation, and mantle dynamics.

5 Conclusion

We have extracted a smoothed estimate of postseismic deformation following the El Mayor-Cucapah earthquake from GPS displacement time series. Our estimated postseismic deformation reveals far-field (epicentral distances $\gtrsim 200$ km) transient deformation which is undetectable after about three years. Near-field deformation exhibits transience that decays to a sustained, elevated rate after about one or two years. We found that near-field transient deformation can be explained with shallow afterslip. The sustained rate of near-field deformation can be explained with viscoelastic relaxation in the lower crust and possibly continued afterslip. Far-field transient deformation can be more definitively ascribed to viscoelastic relaxation at depths greater than ~ 60 km. Beneath that depth, a transient viscosity of $\sim 1 \times 10^{18}$ Pa s is required to describe the rate of far-field deformation throughout the five years considered in this study. By describing the available postseismic deformation with a transient rheology in the mantle, our preferred model does not conflict with the generally higher steady-state viscosities inferred from geophysical processes occurring over longer time scales.

Acknowledgements

We thank Andy Freed for an illuminating discussion on the data used in this study. We thank Fred Pollitz and an anonymous reviewer for comments that improved this manuscript. We also thank the editor, Martha Savage. This material is based on EarthScope Plate Boundary Observatory data services provided by UNAVCO through the GAGE Facility with support from the National Science Foundation (NSF) and National Aeronautics and Space Administration (NASA) under NSF Cooperative Agreement No. EAR-1261833. The data used in this study can be found at www.unavco.org. This material is based upon work supported by the National Science Foundation under Grant Numbers EAR 1045372 and EAR 1245263.

References

- 657 Aagaard, B. T., M. G. Knepley, and C. A. Williams (2013), A domain decomposition
658 approach to implementing fault slip in finite-element models of quasi-static and dy-
659 namic crustal deformation, *Journal of Geophysical Research: Solid Earth*, 118, doi:
660 10.1002/jgrb.50217.
- 661 Argus, D. F., M. B. Heflin, G. Peltzer, F. Crampé, and F. H. Webb (2005), Interseismic
662 strain accumulation and anthropogenic motion in metropolitan Los Angeles, *Journal of*
663 *Geophysical Research: Solid Earth*, 110(B04401), 1–26, doi:10.1029/2003JB002934.
- 664 Aster, R. C., B. Borchers, and C. H. Thurber (2011), Parameter Estimation and Inverse
665 Problems, vol. 90, Academic Press.
- 666 Bawden, G. W., W. Thatcher, R. S. Stein, K. W. Hudnut, and G. Peltzer (2001), Tectonic
667 contraction across Los Angeles after removal of groundwater pumping effects., *Nature*,
668 412, 812–815, doi:10.1038/35090558.
- 669 Bills, B. G., and G. M. May (1987), Lake Bonneville: Constraints on Lithospheric Thick-
670 ness and Upper Mantle Viscosity From Isostatic Warping of Bonneville, Provo, and

- 671 Gilbert Stage Shorelines, *Journal of Geophysical Research-Solid Earth and Planets*,
 672 92(B11), 11, 11493–11508, doi:10.1029/JB092iB11p11493.
- 673 Çakir, Z., S. Ergintav, H. Özener, U. Dogan, A. M. Akoglu, M. Meghraoui, and
 674 R. Reilinger (2012), Onset of aseismic creep on major strike-slip faults, *Geology*,
 675 40(12), 1115–1118, doi:10.1130/G33522.1.
- 676 Cavalié, O., M. P. Doin, C. Lasserre, and P. Briole (2007), Ground motion measurement in
 677 the Lake Mead area, Nevada, by differential synthetic aperture radar interferometry time
 678 series analysis: Probing the lithosphere rheological structure, *Journal of Geophysical
 679 Research: Solid Earth*, 112(B03403), 1–18, doi:10.1029/2006JB004344.
- 680 Cetin, E., Z. Çakir, M. Meghraoui, S. Ergintav, and A. M. Akoglu (2014), Extent and
 681 distribution of aseismic slip on the İsmetpaşa segment of the North Anatolian Fault
 682 (Turkey) from Persistent Scatterer InSAR, *Geochemistry, Geophysics, Geosystems*, 15,
 683 doi:10.1002/2014GC005307.
- 684 Chopra, P. N. (1997), High-temperature transient creep in olivine rocks, *Tectonophysics*,
 685 279, 93–111, doi:10.1016/S0040-1951(97)00134-0.
- 686 Crittenden, M. (1967), Viscosity and Finite Strength of the Mantle as Determined from
 687 Water and Ice Loads, *Geophysical Journal of the Royal Astronomical Society*, 261–279,
 688 doi:10.1111/j.1365-246X.1967.tb06243.x.
- 689 Davis, J. L., B. P. Wernicke, and M. E. Tamisiea (2012), On seasonal signals in geodetic
 690 time series, *Journal of Geophysical Research: Solid Earth*, 117(B01403), 1–10, doi:
 691 10.1029/2011JB008690.
- 692 Feigl, K. L., and W. Thatcher (2006), Geodetic observations of post-seismic transients in
 693 the context of the earthquake deformation cycle, *Comptes Rendus - Geoscience*, 338,
 694 1012–1028, doi:10.1016/j.crte.2006.06.006.
- 695 Fletcher, J. M., O. J. Teran, T. K. Rockwell, M. E. Osokin, K. W. Hudnut, K. J. Mueller,
 696 R. M. Spelz, S. O. Akciz, E. Masana, G. Faneros, E. J. Fielding, S. Leprince, A. E.
 697 Morelan, J. Stock, D. K. Lynch, A. J. Elliott, P. Gold, J. Liu-Zeng, A. González-
 698 Ortega, A. Hinojosa-Corona, and J. González-García (2014), Assembly of a large
 699 earthquake from a complex fault system: Surface rupture kinematics of the 4 April
 700 2010 El Mayor-Cucapah (Mexico) Mw 7.2 earthquake, *Geosphere*, 10(4), 797–827,
 701 doi:10.1130/GES00933.1.
- 702 Freed, A. M., R. Bürgmann, E. Calais, J. Freymueller, and S. Hreinsdóttir (2006), Impli-
 703 cations of deformation following the 2002 Denali, Alaska, earthquake for postseismic
 704 relaxation processes and lithospheric rheology, *Journal of Geophysical Research: Solid
 705 Earth*, 111(B01401), 1–23, doi:10.1029/2005JB003894.
- 706 Freed, A. M., R. Bürgmann, and T. Herring (2007), Far-reaching transient motions after
 707 Mojave earthquakes require broad mantle flow beneath a strong crust, *Geophysical
 708 Research Letters*, 34(L19302), 1–5, doi:10.1029/2007GL030959.
- 709 Gonzalez-Ortega, A., Y. Fialko, D. Sandwell, F. A. Nava-pichardo, J. Fletcher,
 710 J. Gonzalez-garcia, B. Lipovsky, M. Floyd, and G. Funning (2014), El Mayor-Cucapah
 711 (Mw7.2) earthquake: early near-field postseismic deformation from InSar and GPS
 712 observations, *Journal of Geophysical Research: Solid Earth*, 119, 1482–1497, doi:
 713 10.1002/2013JB010193.
- 714 Hauksson, E., J. Stock, K. Hutton, W. Yang, J. A. Vidal-Villegas, and H. Kanamori
 715 (2011), The 2010 Mw 7.2 El mayor-cucapah earthquake sequence, Baja California,
 716 Mexico and Southernmost California, USA: Active seismotectonics along the Mexican
 717 pacific margin, *Pure and Applied Geophysics*, 168, 1255–1277, doi:10.1007/s00024-010-
 718 0209-7.
- 719 Hearn, E. H. (2003), What can GPS data tell us about the dynamics of post-seismic
 720 deformation, *Geophysical Journal International*, 115, 753–777, doi:10.1111/j.1365-
 721 246X.2003.02030.x.
- 722 Hearn, E. H., S. McClusky, S. Ergintav, and R. E. Reilinger (2009), Izmit earthquake
 723 postseismic deformation and dynamics of the North Anatolian Fault Zone, *Journal of
 724 Geophysical Research: Solid Earth*, 114(B08405), 1–21, doi:10.1029/2008JB006026.

- Hetland, E. A. (2003), Postseismic relaxation across the Central Nevada Seismic Belt, *Journal of Geophysical Research*, 108(B8), 1–13, doi:10.1029/2002JB002257.
- Hetland, E. A., and G. Zhang (2014), Effect of shear zones on post-seismic deformation with application to the 1997 Mw 7.6 manyi earthquake, *Geophysical Journal International*, 206(2), 1–11, doi:10.1093/gji/ggu127.
- Hines, T. T., and E. A. Hetland (2013), Bias in estimates of lithosphere viscosity from interseismic deformation, *Geophysical Research Letters*, 40(16), 4260–4265, doi:10.1002/grl.50839.
- Hines, T. T., and E. A. Hetland (2016), Rapid and simultaneous estimation of fault slip and heterogeneous lithospheric viscosity from post-seismic deformation, *Geophysical Journal International*, 204(1), 569–582, doi:10.1093/gji/ggv477.
- Jacobs, A., D. Sandwell, Y. Fialko, and L. Sichoux (2002), The 1999 (Mw7.1) Hector Mine, California, Earthquake: Near-Field Postseismic Deformation from ERS Interferometry, *Bulletin of the Seismological Society of America*, 92(4), 1433–1442.
- Johnson, K. M., and P. Segall (2004), Viscoelastic earthquake cycle models with deep stress-driven creep along the San Andreas fault system, *Journal of Geophysical Research: Solid Earth*, 109(B10403), 1–19, doi:10.1029/2004JB003096.
- Johnson, K. M., R. Bürgmann, and J. T. Freymueller (2009), Coupled afterslip and viscoelastic flow following the 2002 Denali Fault, Alaska earthquake, *Geophysical Journal International*, 176(3), 670–682, doi:10.1111/j.1365-246X.2008.04029.x.
- Jónsson, S., P. Segall, R. Pedersen, and G. Bjornsson (2003), Post-earthquake ground movements correlated to pore-pressure transients, *Nature*, 424, 179–183, doi:10.1038/nature01758.1.
- Kaufmann, G., and F. Amelung (2000), Reservoir-induced deformation and continental rheology in vicinity of Lake Mead, Nevada, *Journal of Geophysical Research*, 105(B7), 16,341, doi:10.1029/2000JB900079.
- Kroll, K. A., E. S. Cochran, K. B. Richards-Dinger, and D. F. Sumy (2013), Aftershocks of the 2010 Mw 7.2 El Mayor-Cucapah earthquake reveal complex faulting in the Yuha Desert, California, *Journal of Geophysical Research: Solid Earth*, 118, 6146–6164, doi:10.1002/2013JB010529.
- Lekic, V., S. W. French, and K. M. Fischer (2011), Lithospheric Thinning Beneath Rifted Regions of Southern California, *Science* 334, 783–787.
- Liu, H.-P., D. L. Anderson, and H. Kanamori (1976), Velocity dispersion due to anelasticity; implications for seismology and mantle composition *Geophysical Journal of the Royal Astronomical Society*, 47, 41–58, doi:10.1111/j.1365-246X.1976.tb01261.x.
- Lundgren, P., E. A. Hetland, Z. Liu, and E. J. Fielding (2009), Southern San Andreas-San Jacinto fault system slip rates estimated from earthquake cycle models constrained by GPS and interferometric synthetic aperture radar observations, *Journal of Geophysical Research: Solid Earth* 114(B02403), 1–18, doi:10.1029/2008JB005996.
- McGuire, J. J., and P. Segall (2003), Imaging of aseismic fault slip transients recorded by dense geodetic networks, *Geophysical Journal International*, 155, 778–788, doi:10.1111/j.1365-246X.2003.02022.x.
- Meade, B. J., and B. H. Hager (2005), Block models of crustal motion in southern California constrained by GPS measurements, *Journal of Geophysical Research: Solid Earth*, 110(B03403), 1–19, doi:10.1029/2004JB003209.
- Murray, J. R., and P. Segall (2005), Spatiotemporal evolution of a transient slip event on the San Andreas fault near Parkfield, California, *Journal of Geophysical Research: Solid Earth*, 110(B09407), 1–12, doi:10.1029/2005JB003651.
- Nur, A., and G. Mavko (1974), Postseismic viscoelastic rebound, *Science*, 183(4121), 204–206, doi:10.1038/098448b0.
- O'Connell, R. J. (1971), Rheology of the Mantle, *EOS, Transactions, American Geophysical Union*, 52, 140–142.
- Oskin, M. E., J. R. Arrowsmith, A. Hinojosa Corona, A. J. Elliott, J. M. Fletcher, E. J. Fielding, P. O. Gold, J. J. Gonzalez Garcia, K. W. Hudnut, J. Liu-Zeng, and O. J. Teran

- (2012), Near-field deformation from the El Mayor-Cucapah earthquake revealed by differential LIDAR, *Science*, 335, 702–705, doi:10.1126/science.1213778.
- Pollitz, F., C. Wicks, and W. Thatcher (2001), Mantle Flow Beneath a Continental Strike-Slip Fault: Postseismic Deformation After the 1999 Hector Mine Earthquake, *Science*, 293, 1814–1818, doi:10.1126/science.1061361.
- Pollitz, F. F. (2003), Transient rheology of the uppermost mantle beneath the Mojave Desert, California, *Earth and Planetary Science Letters*, 215, 89–104, doi:10.1016/S0012-821X(03)00432-1.
- Pollitz, F. F., G. Peltzer, and R. Bürgmann (2000), Mobility of continental mantle: Evidence from postseismic geodetic observations following the 1992 Landers earthquake, *Journal of Geophysical Research*, 105(B4), 8035–8054, doi:10.1029/1999JB900380.
- Pollitz, F. F., R. Bürgmann, and W. Thatcher (2012), Illumination of rheological mantle heterogeneity by the M7.2 2010 El Mayor-Cucapah earthquake, *Geochemistry, Geophysics, Geosystems*, 13(6), 1–17, doi:10.1029/2012GC004139.
- Pollitz, F. F. (2015), Postearthquake relaxation evidence for laterally variable viscoelastic structure and water content in the Southern California mantle, *Journal of Geophysical Research: Solid Earth*, 120, 2672–2696, doi:10.1002/2014JB011603.
- Rauch, H. E., F. Tung, and C. T. Striebel (1965), Maximum likelihood estimates of linear dynamic systems, *AIAA Journal*, 3(8), 1445–1450.
- Riva, R. E. M., and R. Govers (2009), Relating viscosities from postseismic relaxation to a realistic viscosity structure for the lithosphere, *Geophysical Journal International*, 176, 614–624, doi:10.1111/j.1365-246X.2008.04004.x.
- Rollins, C., S. Barbot, and J.-P. Avouac (2015), Postseismic Deformation Following the 2010 M7.2 El Mayor-Cucapah Earthquake: Observations, Kinematic Inversions, and Dynamic Models, *Pure and Applied Geophysics*, 172(5), 1305–1358, doi:10.1007/s00024-014-1005-6.
- Savage, J. C. (1990), Equivalent strike-slip earthquake cycles in half-space and lithosphere-asthenosphere earth models, *Journal of Geophysical Research*, 95(B4), 4873–4879, doi:10.1029/JB095iB04p04873.
- Savage, J. C., and J. L. Svart (2009), Postseismic relaxation following the 1992 M7.3 Landers and 1999 M7.1 Hector Mine earthquakes, southern California, *Journal of Geophysical Research*, 114(B01401), doi:10.1029/2008JB005938.
- Savage, J. C., J. L. Svart, and S. B. Yu (2005), Postseismic relaxation and transient creep, *Journal of Geophysical Research: Solid Earth*, 110(B11402), 1–14, doi:10.1029/2005JB003687.
- Segall, P., and M. Mathews (1997), Time dependent inversion of geodetic data, *Journal of Geophysical Research*, 102(B10), 22391–22409.
- Spinler, J. C., R. A. Bennett, C. Walls, L. Shawn, and J. J. G. Garcia (2015), Assessing long-term postseismic deformation following the M7.2 4 April 2010, El Mayor-Cucapah earthquake with implications for lithospheric rheology in the Salton Trough, *Journal of Geophysical Research: Solid Earth*, 120, 3664–3679, doi:10.1002/2014JB011613.
- Wei, M., D. Sandwell, Y. Fialko, and R. Bilham (2011a), Slip on faults in the Imperial Valley triggered by the 4 April 2010 Mw 7.2 El Mayor-Cucapah earthquake revealed by InSAR, *Geophysical Research Letters*, 38(L01308), 1–6 doi:10.1029/2010GL045235.
- Wei, M., Y. Liu, Y. Kaneko, J. J. McGuire, and R. Bilham (2015), Dynamic triggering of creep events in the Salton Trough, Southern California by regional M5.4 earthquakes constrained by geodetic observations and numerical simulations, *Earth and Planetary Science Letters*, 427, 1–10, doi:10.1016/j.epsl.2015.06.044.
- Wei, S., E. Fielding, S. Leprince, A. Sladen, J.-P. Avouac, D. Helmberger, E. Hauksson, R. Chu, M. Simons, K. Hudnut, T. Herring, and R. Briggs, (2011b), Superficial simplicity of the 2010 El MayorCucapah earthquake of Baja California in Mexico, *Nature Geoscience*, 4, 615–618, doi:10.1038/ngeo1213.
- Yang M., and M. N. Toksöz (1981), Time-dependent deformation and stress relaxation after strike-slip earthquakes, *Journal of Geophysical Research*, 86, 2889–2901.

- 833 Yuen, D. A., and W. R. Peltier (1982), Normal modes of the viscoelastic earth, *Geo-*
834 *physical Journal of the Royal Astronomical Society*, 69, 495–526, doi:10.1111/j.1365-
835 246X.1982.tb04962.x.

Supporting Information for “Rheologic constraints on the upper mantle from five years of postseismic deformation following the El Mayor-Cucapah earthquake”

Trevor T. Hines,¹ Eric A. Hetland,¹

Contents of this file

1. Figures S1 to S4

Introduction

Figures S1 and S2 provide additional information about the inversion in Section 3.2 of the main text. Figures S3 and S4 show the predicted displacements, which have been decomposed into elastic and viscoelastic components, for the preferred model from Section 3.3.

Corresponding author: T. T. Hines, Department of Earth and Environmental Sciences, University of Michigan, 2534 C. C. Little Building, 1100 North University Avenue, Ann Arbor, MI 48109-1005. (hinest@umich.edu)

¹Department of Earth and Environmental Sciences, University of Michigan, Ann Arbor, Michigan, USA.

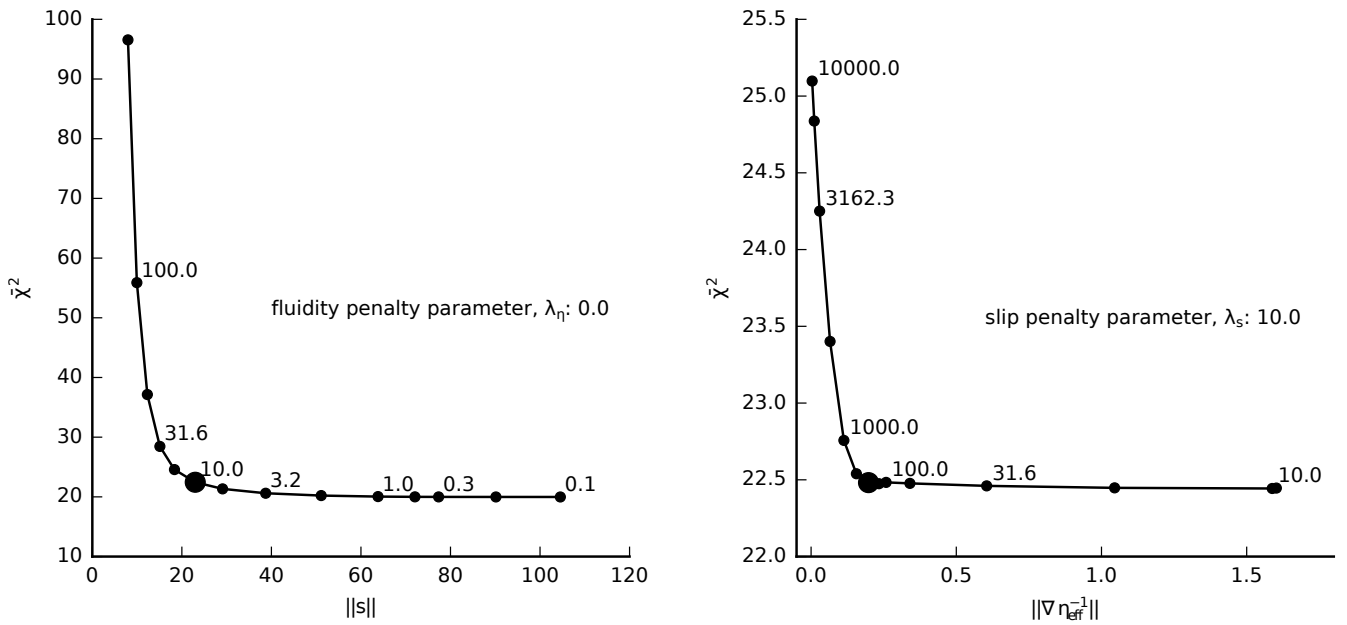


Figure S1. Trade-off curves used to determine the damping parameters λ_s and λ_η in eq. (15)

of the main text. The left panel shows the trade-off curve for the fault slip penalty parameter, λ_s . We pick λ_s while keeping the penalty parameter for fluidity, λ_η , fixed at zero. The right panel shows the trade-off curve for selecting λ_η , where we fix λ_s at the chosen value from the left panel. Chosen values are indicated with the larger marker. When picking λ_s , we try to find a good balance between the mean chi-squared value, $\bar{\chi}^2$, and the size of the slip parameters, $\|s\|$. Our choice of λ_η is a balance between $\bar{\chi}^2$ and the size of the Laplacian of fluidity, $\|\nabla \eta_{\text{eff}}^{-1}\|$.

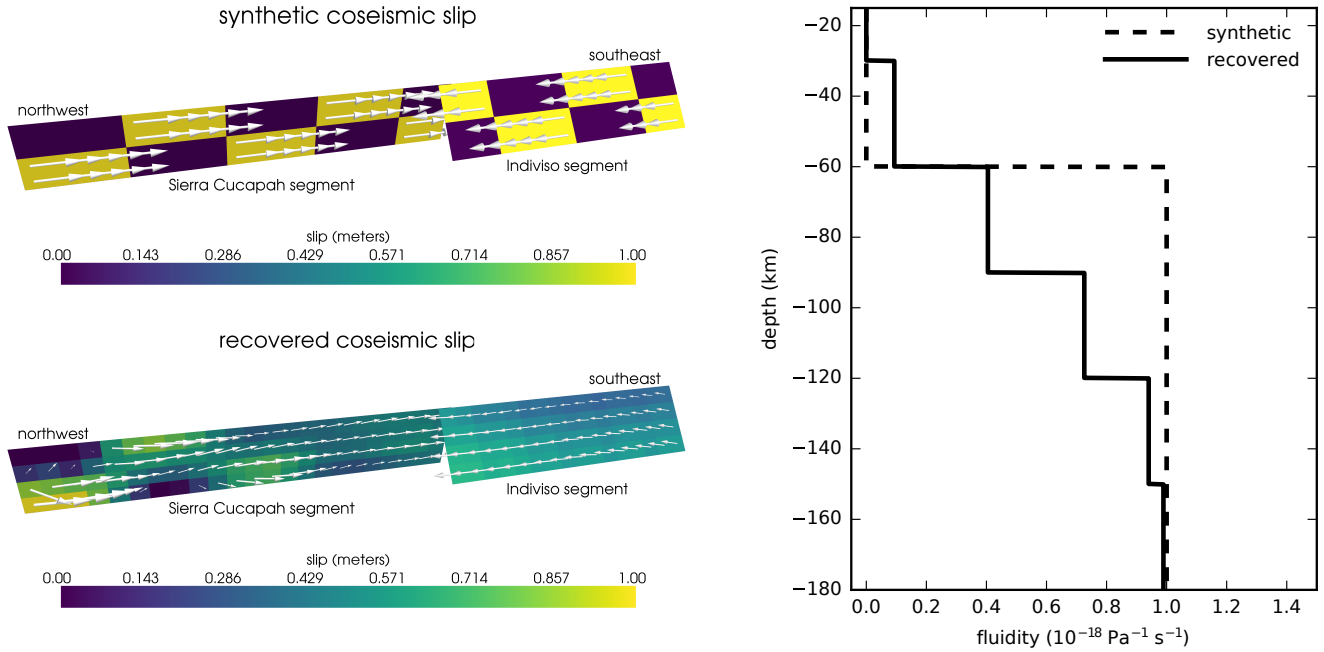


Figure S2. Checkerboard test used to assess the resolving power of the inversion in Section 3.2 of the main text. We create synthetic data at all of the GPS stations considered in this study by evaluating eq. (14) with the synthetic coseismic slip distribution and fluidity distributions. Our synthetic fluidity model has a jump from 0.0 to $10^{-18} \text{ Pa}^{-1} \text{ s}^{-1}$ at 60 km depth. Our synthetic slip model does not include afterslip, although we estimate afterslip along with coseismic slip and fluidity in this test. We estimate these values in the same way as described in the main text and we also use the same penalty parameters. We do not add any noise to our synthetic data so that the recovered model just indicates how much the regularization influences the solution. Note that our ability to recover slip decreases towards the southern end of the fault, farthest from the available data. Also note that the smoothing constraint on fluidity largely obscures the jump in the synthetic model.

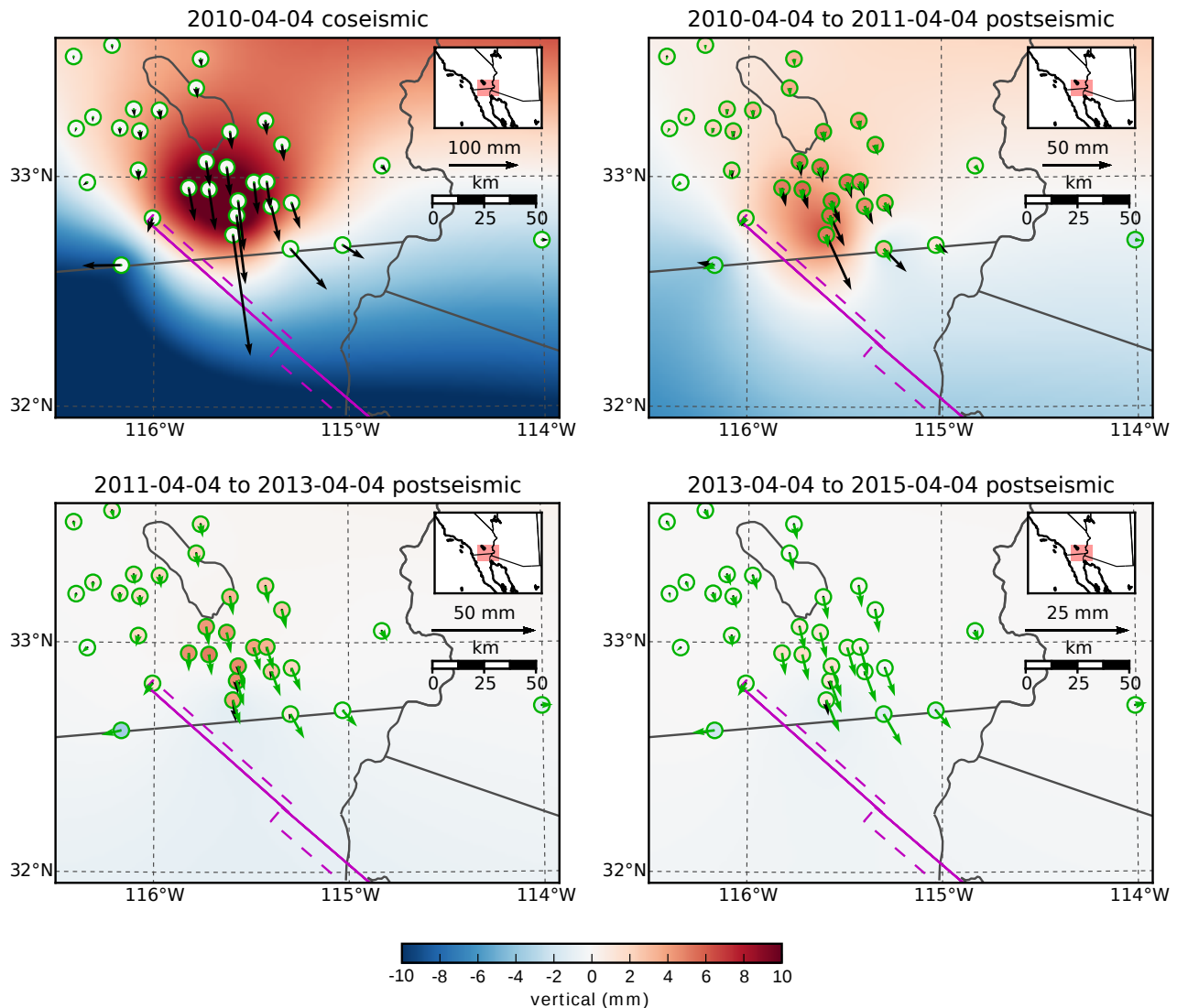


Figure S3. Elastic (black) and viscoelastic (green) components of the near-field predicted displacements for the preferred Zener model from Section 3.3. The elastic component is the deformation resulting from fault slip and the viscoelastic component is the deformation resulting from viscoelastic relaxation of stresses induced by the fault slip. The elastic and viscoelastic components are calculated from the first and second terms in eq. (11), respectively. The vertical elastic component is shown as an interpolated field and the vertical viscoelastic component is shown within the green circles.

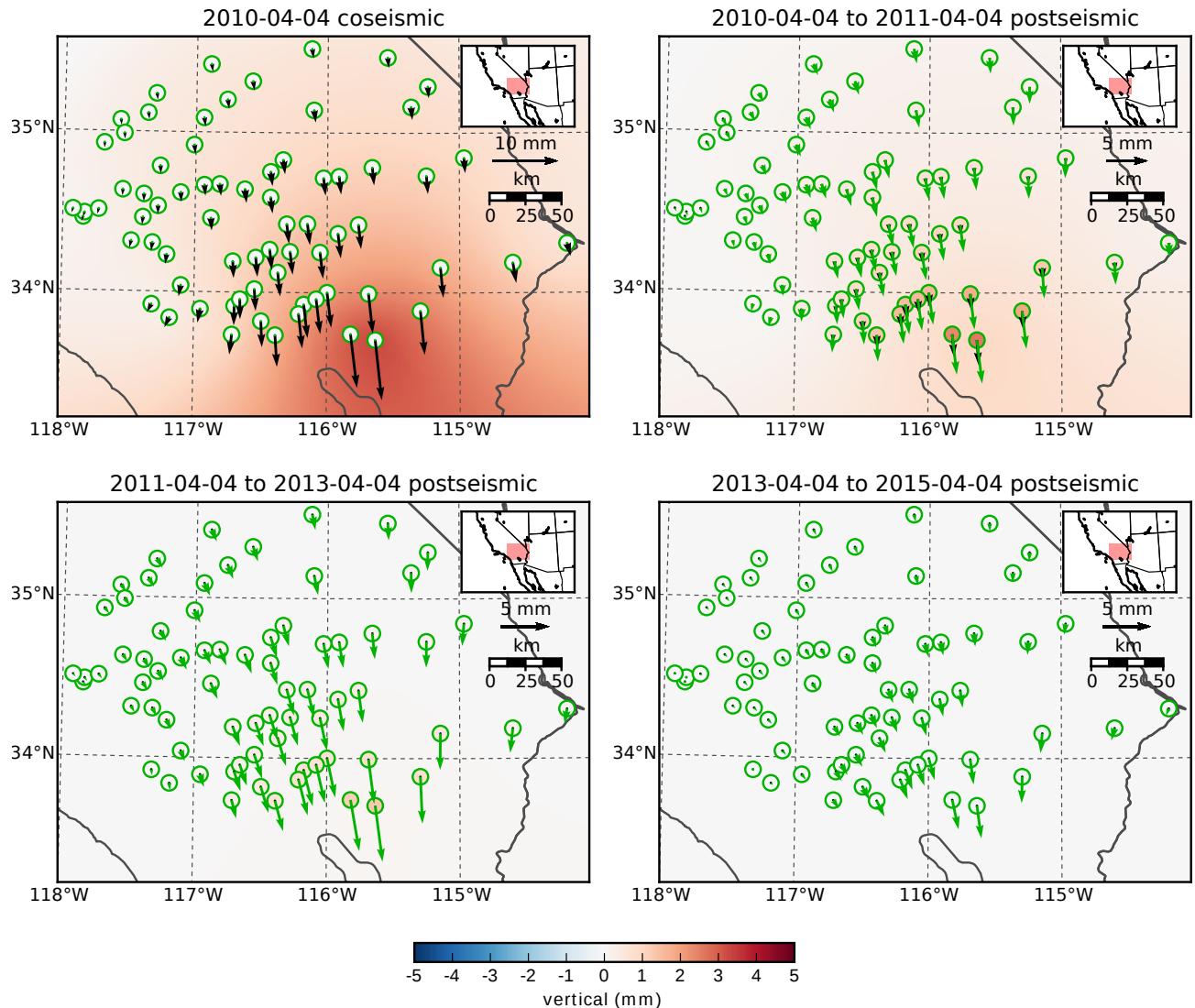


Figure S4. Same as figure S3 but for far-field stations.